

Kinetic Energy Budget during the Genesis Period of Tropical Cyclone Durian (2001) in the South China Sea

YAPING WANG

Key Laboratory of Cloud-Precipitation Physics and Severe Storms (LACS), Institute of Atmospheric Physics, Chinese Academy of Sciences, and University of Chinese Academy of Sciences, Beijing, China

XIAOPENG CUI

Key Laboratory of Cloud-Precipitation Physics and Severe Storms (LACS), Institute of Atmospheric Physics, Chinese Academy of Sciences, Beijing, and Collaborative Innovation Center on Forecast and Evaluation of Meteorological Disasters, Nanjing University of Information Science and Technology, Nanjing, China

XIAOFAN LI

School of Earth Sciences, Zhejiang University, Hangzhou, China

WENLONG ZHANG

Institute of Urban Meteorology, China Meteorological Administration, Beijing, China

YONGJIE HUANG

Key Laboratory of Cloud-Precipitation Physics and Severe Storms (LACS), Institute of Atmospheric Physics, Chinese Academy of Sciences, and University of Chinese Academy of Sciences, Beijing, China

(Manuscript received 4 February 2015, in final form 4 March 2016)

ABSTRACT

A set of kinetic energy (KE) budget equations associated with four horizontal flow components was derived to study the KE characteristics during the genesis of Tropical Cyclone (TC) Durian (2001) in the South China Sea using numerical simulation data. The genesis process was divided into three stages: the monsoon trough stage (stage 1), the midlevel mesoscale convective vortex (MCV) stage (stage 2), and the establishment stage of the TC vortex (stage 3). Analysis showed that the KE of the symmetric rotational flow (SRF) was the largest and kept increasing, especially in stages 2 and 3, representing the symmetrization process during TC genesis. The KE of the SRF was mainly converted from the KE of the symmetric divergent flow (SDF), largely transformed from the available potential energy (APE). It was found that vortical hot towers (VHTs) emerged abundantly, aggregated, and merged within the MCV region in stages 1 and 2. From the energy budget perspective, massive moist-convection-produced latent heat was concentrated and accumulated within the MCV region, especially in stage 2, and further warmed the atmosphere, benefiting the accumulation of APE and the transformation from APE to KE. As a result, the midlevel circulation (or MCV) grew strong rapidly. In stage 3, the intensity and number of VHTs both decreased. However, affected by increasing lower-level inward radial wind, latent heat released by the organized convection, instead of disorganized VHTs in the first two stages, continuously contributed to the strengthening of the surface TC circulation as well as the warm core.

1. Introduction

China is often struck by tropical cyclones (TCs), especially in south and southeast China, where TCs make landfalls most frequently and lead to severe disasters. Tropical cyclone genesis, as an important aspect of TC

Corresponding author address: Dr. Xiaopeng Cui, Key Laboratory of Cloud-Precipitation Physics and Severe Storms (LACS), Institute of Atmospheric Physics, Chinese Academy of Sciences, Beijing 100029, China.
E-mail: xpcui@mail.iap.ac.cn

research and forecasting, has been studied for a long time (Zhang and Cui 2013). The environmental conditions and physical factors associated with TC formations have been analyzed in detail (Palmen 1948; Riehl 1948; Charney and Eliassen 1964; Gray 1968; Emanuel 1986; Rotunno and Emanuel 1987; Cheung 2004; Zhang and Cui 2013). Gray (1968, 1998) proposed six factors favorable for tropical disturbance and storm development: sufficient displacement away from the equator, low-level relative vorticity, weak vertical wind shear, relatively high underlying sea surface temperature, a deep layer of conditional instability, and abundant moisture in the middle troposphere. Cheung (2004) obtained six large-scale parameters for tropical cyclone formation: the sea surface temperature, 200–850-hPa vertical and meridional zonal shear, 500–700-hPa average relative humidity, convective available potential energy, and 200-hPa divergence, based on which a formation potential area was defined. Charney and Eliassen (1964) pointed out that cyclones develop by conditional instability of the second kind (CISK), in which cumulus convection supplies latent heat to the cyclone and the cyclone supplies moisture to the convection. Emanuel (1986) and Rotunno and Emanuel (1987) proposed the wind-induced surface heat exchange (WISHE) mechanism, suggesting that the intensification and maintenance of TCs depend on air-sea latent and sensible heat transfer, and are the result of a finite-amplitude air-sea interaction instability. Both CISK and WISHE require that an initial low pressure vortex with certain intensity already exists, and may not be suitable for explaining formations of TCs. Tropical cyclone genesis is actually an evolutionary process from disorganized tropical disturbances to initial low pressure vortices (Zehr 1992), which is still not well understood.

In the 1990s, interactions between synoptic-scale circulations and mesoscale convective activities during TC formations were studied (Ritchie and Holland 1997, 1999). The mesoscale characteristics of the transformation from mesoscale convective systems (MCS) into TCs were also investigated. Lee et al. (2008) pointed out that monsoon-related formations have the highest percentage of coexisting MCS, so the interaction between these systems may play a role in the TC formation process. Some studies (Zehr 1992; Zhang and Bao 1996; Bister and Emanuel 1997; Zhang et al. 2008b, 2010) have suggested that the formation of a midlevel mesoscale convective vortex (MCV) in the stratiform precipitation area of MCS is the precursor to TC genesis. Bister and Emanuel (1997) postulated a mechanism for the development of Hurricane Guillermo based on data observed during the Tropical Experiment in Mexico (TEXMEX) and from numerical

simulations, that is, a midlevel MCV, driven by the stratiform rain, expands downward and brings cold, humidified air to the boundary layer. With the redevelopment of convection, a near-surface warm-core cyclone develops. This is so-called top-down thinking. In contrast to top-down thinking, a different hypothesis called bottom-up thinking is also proposed, in which the surface-based convection or vortical hot towers (VHTs) play a key role. VHTs are horizontally small (about 10–30 km) but intense cumulonimbus convection cores that can reach the tropopause via nearly undiluted ascent (Montgomery et al. 2006). In bottom-up thinking, the warm-core formation and near-surface tangential momentum spinup are accelerated by the VHT organization process, which can effectively trap and aggregate the latent heat from moist convection (Hendricks et al. 2004; Montgomery et al. 2006). Both top-down and bottom-up thinking describe the vorticity growth mechanism during TC genesis. Our previous work (Zhang et al. 2010) preliminarily explored the related mechanism of TC genesis, showing that the cyclonic vorticity grew in the lower and middle troposphere, and that the low-level vorticity grew more rapidly. Though the maximum vorticity core moves from the mid-to low level, it cannot be concluded that the MCV directly transfers vorticity to the low level, which is the main idea of top-down thinking. Therefore, tropical cyclogenesis is still an outstanding issue.

Studies on TCs in the South China Sea (SCS) have attracted increasing attention recently. Tropical cyclones forming over the relatively narrow SCS often present rapid development rates, erratic tracks, and short life cycles (Yi et al. 2008), which can exert distinct and quick impacts on China, especially south China and the SCS. Thus, better understanding of the formation processes and more accurate predictions of TC tracks and intensities in the SCS will be of great help in reducing economic losses and guaranteeing securities (Zhang and Guo 2008; Zhang and Cui 2013; Wang et al. 2013). Wang and Lau (2011) statistically analyzed tropical disturbances during 1997–2006 in the SCS, pointing out that total annual numbers of tropical disturbances and developing tropical disturbances over the SCS decreased while the development rates of tropical disturbances increased. Using the high-resolution ECMWF/Year of Tropical Convection (YOTC) analyses and multiple satellite observations, Park et al. (2015) pointed out that the interactions between multispatial and temporal scales of tropical circulations can explain how tropical disturbances transformed into TCs. Mekkhala (2008). Lee et al. (2006) examined TC formations in the SCS and compared the TCs associated with a weak baroclinic environment of a mei-yu front and TCs

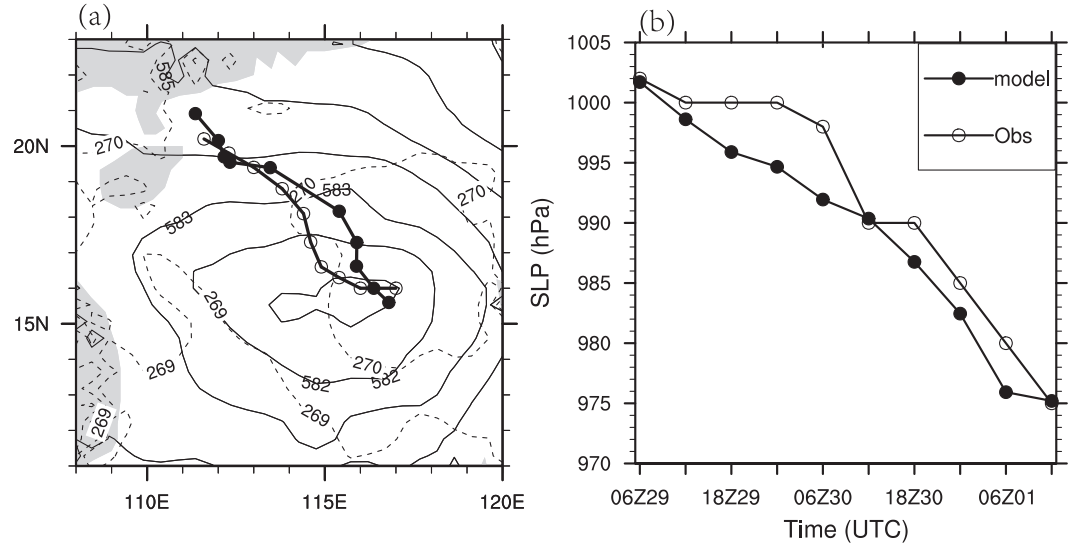


FIG. 1. (a) Simulated and observed track of TC Durian from 0600 UTC 29 Jun to 1200 UTC 1 Jul 2001. The thick solid line with 6-hourly positions marked by filled (empty) circles denotes the simulated (observed) track. Contours: simulated 500-hPa geopotential height (solid line, unit: dgpm) and temperature (dashed line, unit: K) at 0900 UTC 29 Jun. (b) Simulated and observed intensity of Durian from 0600 UTC 29 Jun to 1200 UTC 1 Jul 2001.

without a front. The results showed that a nonfrontal formation usually occurs at lower latitudes, is more barotropic, develops faster, and possibly intensifies into a stronger TC. Zhang et al. (2008a,b, 2010) investigated the effects of the MCV and revealed the typical features of VHTs during the genesis of Durian (2001) using the MM5 model, which will be introduced in detail in section 3.

Energy budget analysis is often used in TC research (Ding and Liu 1985a; Li et al. 2005; Feng et al. 2014; J. Peng et al. 2014; M. S. Peng et al. 2014). Horizontal flows of TCs can be divided into divergent and rotational components. Some research (Chen and Wiin-Nielsen 1976; Ding and Liu 1985b) diagnosed the kinetic energies (KEs) of divergent and nondivergent components of TCs, pointing out that total potential energy is converted into the KE of divergent flow, which is in turn converted into the KE of rotational flow. Furthermore, energy budget analysis of the asymmetric rotational flow of TCs, which is closely related to the interaction between the environmental and symmetric flows of TCs, is also used to examine TC motion (Li and Wang 1994; Chan and Cheung 1998).

Previous energy budget analysis studies have mainly focused on the KE budgets during the period of TC intensification instead of the KE budgets during TC genesis. As mentioned above, TC genesis can be depicted as a transformation (evolutionary) process from disorganized tropical disturbances (small scale, often observed in the tropics) to a close to axisymmetric,

self-sustaining, and organized synoptic-scale vortex (TC). The formation and development of the synoptic-scale cyclonic vortex (TC) is accompanied by an increase of the associated KEs (especially axisymmetric rotational KE). The increase in axisymmetric rotational KE is closely related to the transformations between KEs and potential energies and conversions between various KE components associated with different flow components (symmetric flow, asymmetric flow, divergent flow, and rotational flow). The understanding of the above transformation (conversion) physical processes could help us to better understand the TC genesis process (the increase of the axisymmetric rotational KE associated with the establishment of TC circulations). Few studies on these topics have been conducted due to a lack of observations and difficulties in simulating TC genesis. In this study, KE budget analysis is applied to diagnose the genesis process of TC Durian (2001) in the SCS. The main aim of this study was to improve our understanding of the above transformation (conversion) processes and the TC genesis process through detailed budget analysis using a rather good simulation of a TC genesis. Furthermore, based on KE analysis, the major systems were revealed, as well as the possible causes of their variation from the aspect of energetics, which could help to further understand the kinematic properties during tropical cyclogenesis. As the symmetric rotational flow is closely related to the axisymmetrization process in TC genesis, the horizontal flow was divided into four components: symmetric divergent flow (SDF),

asymmetric divergent flow (ADF), symmetric rotational flow (SRF), and asymmetric rotational flow (ARF). Questions answered include the following: What are the main characteristics of the KE budgets during the TC genesis? What are the main terms contributing to the KE tendency associated with TC Durian's formation?

2. Data and methodology

The data used in this study were obtained from the numerical simulation of the genesis process of TC Durian by Zhang et al. (2008b) using the MM5 model with three nested domains, in which the horizontal resolutions were 54, 18, and 6 km. The model was initiated by analysis fields dominated by a monsoon trough and output the 6-km-resolution data every 20 min. The simulation has been verified in detail in Zhang et al. (2008b), showing that the model reproduces very well the genesis process of Durian from disorganized tropical disturbances to an initial TC vortex (tropical depression), as well as the development of Durian after its genesis. The simulated TC genesis moment was about three hours later (0900 UTC 29 June 2001) than the observed (0600 UTC 29 June 2001), with a genesis

location deviation less than 50 km. Durian's simulated track and moving speed in the subsequent two days were mostly consistent with observations [Fig. 1a; see also Fig. 5 in Zhang et al. (2008b)]. Furthermore, both the evolutions of simulated minimum sea level pressure and maximum surface wind speed near the TC center were in good agreement with observations [Fig. 1b; see also Fig. 6 in Zhang et al. (2008b)], developing from a tropical depression to a tropical storm, and eventually reaching typhoon intensity. In this study, the above-described simulation data were used to analyze the KE budgets during the genesis process of Durian.

Based on previous studies (Kornegay and Vincent 1976; Buechler and Fuelberg 1986; Li and Wang 1994), a set of KE budget equations were derived for this study. The horizontal flow \mathbf{V} was partitioned into symmetric \mathbf{V}_s and asymmetric \mathbf{V}_a components. Then the symmetric and asymmetric flows were further decomposed into rotational ($\mathbf{V}_{\psi_s}, \mathbf{V}_{\psi_a}$) and divergent ($\mathbf{V}_{\chi_s}, \mathbf{V}_{\chi_a}$) components using the iterative method of directly calculating streamfunctions (ψ_s, ψ_a) and velocity potentials (χ_s, χ_a) from a wind field based on Endlich's method (Li et al. 2012). The four KE budget equations averaged in a circular domain are written as follows:

$$\begin{aligned} \frac{\partial K_{\psi_s}}{\partial t} &= \left\langle \left[-(\mathbf{V} \cdot \nabla \mathbf{V}_{\psi_a}) \cdot \mathbf{V}_{\psi_s} - \omega \frac{\partial \mathbf{V}_{\psi_a}}{\partial p} \cdot \mathbf{V}_{\psi_s} - f \mathbf{k} \cdot \nabla \psi_a \times \nabla \psi_s \right] \right\rangle + \left\langle \left[-(\mathbf{V} \cdot \nabla \mathbf{V}_{\chi_s}) \cdot \mathbf{V}_{\psi_s} - \omega \frac{\partial \mathbf{V}_{\chi_s}}{\partial p} \cdot \mathbf{V}_{\psi_s} - f \nabla \chi_s \cdot \nabla \psi_s \right] \right\rangle \\ DK_{\psi_s} &\quad (K_{\psi_a}, K_{\psi_s}) \\ &+ \left\langle \left[-(\mathbf{V} \cdot \nabla \mathbf{V}_{\chi_a}) \cdot \mathbf{V}_{\psi_s} - \omega \frac{\partial \mathbf{V}_{\chi_a}}{\partial p} \cdot \mathbf{V}_{\psi_s} - f \nabla \chi_a \cdot \nabla \psi_s \right] \right\rangle - \left\langle \left(\nabla \cdot \mathbf{V} k_{\psi_s} + \frac{\partial \omega k_{\psi_s}}{\partial p} \right) \right\rangle \\ &\quad (K_{\chi_a}, K_{\psi_s}) \\ &+ \langle (\mathbf{F} \cdot \mathbf{V}_{\psi_s}) \rangle - \langle (\nabla \phi \cdot \mathbf{V}_{\psi_s}) \rangle - \left\langle \left(\frac{\partial \mathbf{V}_{\psi_a}}{\partial t} \cdot \mathbf{V}_{\psi_s} + \frac{\partial \mathbf{V}_{\chi_s}}{\partial t} \cdot \mathbf{V}_{\psi_s} + \frac{\partial \mathbf{V}_{\chi_a}}{\partial t} \cdot \mathbf{V}_{\psi_s} \right) \right\rangle, \\ D_{\psi_s} &\quad P_{\psi_s} \quad R_{\psi_s} \\ F_{\psi_s} &\quad (1a) \end{aligned}$$

$$\begin{aligned} \frac{\partial K_{\psi_a}}{\partial t} &= \left\langle \left[-(\mathbf{V} \cdot \nabla \mathbf{V}_{\chi_s}) \cdot \mathbf{V}_{\psi_a} - \omega \frac{\partial \mathbf{V}_{\chi_s}}{\partial p} \cdot \mathbf{V}_{\psi_a} - f \nabla \chi_s \cdot \nabla \psi_a \right] \right\rangle + \left\langle \left[-(\mathbf{V} \cdot \nabla \mathbf{V}_{\chi_a}) \cdot \mathbf{V}_{\psi_a} - \omega \frac{\partial \mathbf{V}_{\chi_a}}{\partial p} \cdot \mathbf{V}_{\psi_a} - f \nabla \chi_a \cdot \nabla \psi_a \right] \right\rangle \\ DK_{\psi_a} &\quad (K_{\chi_s}, K_{\psi_a}) \\ &- \left\langle \left[-(\mathbf{V} \cdot \nabla \mathbf{V}_{\psi_a}) \cdot \mathbf{V}_{\psi_s} - \omega \frac{\partial \mathbf{V}_{\psi_a}}{\partial p} \cdot \mathbf{V}_{\psi_s} - f \mathbf{k} \cdot \nabla \psi_a \times \nabla \psi_s \right] \right\rangle + \left\langle \left[-\mathbf{V} \cdot \nabla (\mathbf{V}_{\psi_s} \cdot \mathbf{V}_{\psi_a}) - \omega \frac{\partial (\mathbf{V}_{\psi_s} \cdot \mathbf{V}_{\psi_a})}{\partial p} \right] \right\rangle \\ &\quad (K_{\psi_a}, K_{\psi_s}) \\ &- \left\langle \left(\nabla \cdot \mathbf{V} k_{\psi_a} + \frac{\partial \omega k_{\psi_a}}{\partial p} \right) \right\rangle + \langle (\mathbf{F} \cdot \mathbf{V}_{\psi_a}) \rangle - \langle (\nabla \phi \cdot \mathbf{V}_{\psi_a}) \rangle - \left\langle \left(\frac{\partial \mathbf{V}_{\psi_s}}{\partial t} \cdot \mathbf{V}_{\psi_a} + \frac{\partial \mathbf{V}_{\chi_s}}{\partial t} \cdot \mathbf{V}_{\psi_a} + \frac{\partial \mathbf{V}_{\chi_a}}{\partial t} \cdot \mathbf{V}_{\psi_a} \right) \right\rangle, \\ F_{\psi_a} &\quad D_{\psi_a} \quad P_{\psi_a} \quad R_{\psi_a} \\ A_{\psi_a} &\quad (1b) \end{aligned}$$

$$\begin{aligned}
\frac{\partial}{\partial t} K_{\chi_s} &= - \left\langle \left[-(\mathbf{V} \cdot \nabla \mathbf{V}_{\chi_s}) \cdot \mathbf{V}_{\psi_s} - \omega \frac{\partial \mathbf{V}_{\chi_s}}{\partial p} \cdot \mathbf{V}_{\psi_s} - f \nabla \chi_s \cdot \nabla \psi_s \right] \right\rangle - \left\langle \left[-(\mathbf{V} \cdot \nabla \mathbf{V}_{\chi_s}) \cdot \mathbf{V}_{\psi_a} - \omega \frac{\partial \mathbf{V}_{\chi_s}}{\partial p} \cdot \mathbf{V}_{\psi_a} - f \nabla \chi_s \cdot \nabla \psi_a \right] \right\rangle \\
DK_{\chi_s} &\quad -(K_{\chi_s}, K_{\psi_s}) \\
&+ \left\langle \left[-(\mathbf{V} \cdot \nabla \mathbf{V}_{\chi_a}) \cdot \mathbf{V}_{\chi_s} - \omega \frac{\partial \mathbf{V}_{\chi_a}}{\partial p} \cdot \mathbf{V}_{\chi_s} - f \mathbf{k} \cdot \nabla \chi_a \times \nabla \chi_s \right] \right\rangle - \left\langle \left(\nabla \cdot \mathbf{V} k_{\chi_s} + \frac{\partial \omega k_{\chi_s}}{\partial p} \right) \right\rangle \\
&\quad -(K_{\chi_s}, K_{\psi_a}) \\
&+ \langle (\mathbf{F} \cdot \mathbf{V}_{\chi_s}) \rangle - \langle (\nabla \phi \cdot \mathbf{V}_{\chi_s}) \rangle - \left\langle \left(\frac{\partial \mathbf{V}_{\chi_a}}{\partial t} \cdot \mathbf{V}_{\chi_s} + \frac{\partial \mathbf{V}_{\psi_s}}{\partial t} \cdot \mathbf{V}_{\chi_s} + \frac{\partial \mathbf{V}_{\psi_a}}{\partial t} \cdot \mathbf{V}_{\chi_s} \right) \right\rangle, \\
D_{\chi_s} &\quad P_{\chi_s} \quad R_{\chi_s}
\end{aligned} \tag{1c}$$

$$\begin{aligned}
\frac{\partial}{\partial t} K_{\chi_a} &= - \left\langle \left[-(\mathbf{V} \cdot \nabla \mathbf{V}_{\chi_a}) \cdot \mathbf{V}_{\psi_s} - \omega \frac{\partial \mathbf{V}_{\chi_a}}{\partial p} \cdot \mathbf{V}_{\psi_s} - f \nabla \chi_a \cdot \nabla \psi_s \right] \right\rangle - \left\langle \left[-(\mathbf{V} \cdot \nabla \mathbf{V}_{\chi_a}) \cdot \mathbf{V}_{\psi_a} - \omega \frac{\partial \mathbf{V}_{\chi_a}}{\partial p} \cdot \mathbf{V}_{\psi_a} - f \nabla \chi_a \cdot \nabla \psi_a \right] \right\rangle \\
DK_{\chi_a} &\quad -(K_{\chi_a}, K_{\psi_s}) \\
&- \left\langle \left[-(\mathbf{V} \cdot \nabla \mathbf{V}_{\chi_a}) \cdot \mathbf{V}_{\chi_s} - \omega \frac{\partial \mathbf{V}_{\chi_a}}{\partial p} \cdot \mathbf{V}_{\chi_s} - f \mathbf{k} \cdot \nabla \chi_a \times \nabla \chi_s \right] \right\rangle + \left\langle \left[-\mathbf{V} \cdot \nabla (\mathbf{V}_{\chi_s} \cdot \mathbf{V}_{\chi_a}) - \omega \frac{\partial (\mathbf{V}_{\chi_s} \cdot \mathbf{V}_{\chi_a})}{\partial p} \right] \right\rangle \\
&\quad -(K_{\chi_a}, K_{\psi_a}) \\
&- \left\langle \left(\nabla \cdot \mathbf{V} k_{\chi_a} + \frac{\partial \omega k_{\chi_a}}{\partial p} \right) \right\rangle + \langle (\mathbf{F} \cdot \mathbf{V}_{\chi_a}) \rangle - \langle (\nabla \phi \cdot \mathbf{V}_{\chi_a}) \rangle - \left\langle \left(\frac{\partial \mathbf{V}_{\chi_s}}{\partial t} \cdot \mathbf{V}_{\chi_a} + \frac{\partial \mathbf{V}_{\psi_s}}{\partial t} \cdot \mathbf{V}_{\chi_a} + \frac{\partial \mathbf{V}_{\psi_a}}{\partial t} \cdot \mathbf{V}_{\chi_a} \right) \right\rangle, \\
F_{\chi_a} &\quad D_{\chi_a} \quad P_{\chi_a} \quad R_{\chi_a}
\end{aligned} \tag{1d}$$

where \mathbf{V} is the horizontal velocity vector, ω is the vertical pressure velocity, \mathbf{F} is the friction force per unit mass, ϕ is the geopotential, f is the Coriolis parameter, k is the horizontal KE per unit mass, and K is the integrated horizontal KE in terms of

$$K_{\psi_s} = \langle (k_{\psi_s}) \rangle = \left\langle \left(\frac{\mathbf{V}_{\psi_s}^2}{2} \right) \right\rangle, \tag{2a}$$

$$K_{\psi_a} = \langle (k_{\psi_a}) \rangle = \left\langle \left(\frac{\mathbf{V}_{\psi_a}^2}{2} \right) \right\rangle, \tag{2b}$$

$$K_{\chi_s} = \langle (k_{\chi_s}) \rangle = \left\langle \left(\frac{\mathbf{V}_{\chi_s}^2}{2} \right) \right\rangle, \tag{2c}$$

$$K_{\chi_a} = \langle (k_{\chi_a}) \rangle = \left\langle \left(\frac{\mathbf{V}_{\chi_a}^2}{2} \right) \right\rangle. \tag{2d}$$

The angle brackets imply an area average as follows:

$$\langle (\cdot) \rangle = \frac{\int_0^{r_0} r dr \int_0^{2\pi} \rho(\cdot) d\lambda}{\pi r_0^2}, \tag{3}$$

where ρ is air density, and r_0 is the radius of the averaging domain and the vortex center, which varies with the time selected as the center.

The KE budget equations of the four wind components can be further written as follows:

$$\begin{aligned}
DK_{\psi_s} &= (K_{\psi_a}, K_{\psi_s}) + (K_{\chi_s}, K_{\psi_s}) + (K_{\chi_a}, K_{\psi_s}) \\
&\quad + F_{\psi_s} + D_{\psi_s} + P_{\psi_s} + R_{\psi_s},
\end{aligned} \tag{4a}$$

$$\begin{aligned}
DK_{\psi_a} &= (K_{\chi_s}, K_{\psi_a}) + (K_{\chi_a}, K_{\psi_a}) - (K_{\psi_a}, K_{\psi_s}) \\
&\quad + A_{\psi_a} + F_{\psi_a} + D_{\psi_a} + P_{\psi_a} + R_{\psi_a},
\end{aligned} \tag{4b}$$

$$\begin{aligned}
DK_{\chi_s} &= -(K_{\chi_s}, K_{\psi_s}) - (K_{\chi_s}, K_{\psi_a}) + (K_{\chi_a}, K_{\chi_s}) \\
&\quad + F_{\chi_s} + D_{\chi_s} + P_{\chi_s} + R_{\chi_s},
\end{aligned} \tag{4c}$$

$$\begin{aligned}
DK_{\chi_a} &= -(K_{\chi_a}, K_{\psi_s}) - (K_{\chi_a}, K_{\psi_a}) - (K_{\chi_a}, K_{\chi_s}) \\
&\quad + A_{\chi_a} + F_{\chi_a} + D_{\chi_a} + P_{\chi_a} + R_{\chi_a},
\end{aligned} \tag{4d}$$

where DK is the KE tendency of each flow component. The conversion term (K_1, K_2) means that KE is converted from flow component 1 to component 2. The terms F_{ψ_s} , F_{ψ_a} , F_{χ_s} , and F_{χ_a} are flux divergence of the four KEs, respectively. The terms P_{ψ_s} , P_{ψ_a} , P_{χ_s} , and P_{χ_a} are

the KEs transformed from potential energies due to cross-contour flows. The terms R_{ψ_s} , R_{ψ_a} , R_{χ_s} , and R_{χ_a} are the KE sources and sinks due to interactions between different flow components. The terms A_{ψ_a} and A_{χ_a} are the KE sources and sinks due to the advections (including horizontal and vertical) of the interactions between symmetric and asymmetric flows. The terms D_{ψ_s} , D_{ψ_a} , D_{χ_s} , and D_{χ_a} are the residual terms, including contributions from friction dissipation, the subgrid-scale effect, latent heat release, and random and system errors (Kornegay and Vincent 1976; Sun et al. 2012). Here, the KE conversion terms from one flow to another in each budget equation are summarized as follows:

$$C_{\psi_s} = (K_{\psi_a}, K_{\psi_s}) + (K_{\chi_s}, K_{\psi_s}) + (K_{\chi_a}, K_{\psi_s}), \quad (5a)$$

$$C_{\psi_a} = (K_{\chi_s}, K_{\psi_a}) + (K_{\chi_a}, K_{\psi_a}) - (K_{\psi_a}, K_{\psi_s}), \quad (5b)$$

$$C_{\chi_s} = -(K_{\chi_s}, K_{\psi_s}) - (K_{\chi_s}, K_{\psi_a}) + (K_{\chi_a}, K_{\chi_s}), \quad (5c)$$

$$C_{\chi_a} = -(K_{\chi_a}, K_{\psi_s}) - (K_{\chi_a}, K_{\psi_a}) - (K_{\chi_a}, K_{\chi_s}). \quad (5d)$$

The KE conversion terms from ARF (K_{ψ_a}), SDF (K_{χ_s}), and ADF (K_{χ_a}) to SRF (K_{ψ_s}) in Eq. (5a) can be further divided as follows:

$$(K_{\psi_a}, K_{\psi_s}) = T_{\psi_a 1} + T_{\psi_a 2} + T_{\psi_a 3}, \quad (6a)$$

$$(K_{\chi_s}, K_{\psi_s}) = T_{\chi_s 1} + T_{\chi_s 2} + T_{\chi_s 3}, \quad (6b)$$

$$(K_{\chi_a}, K_{\psi_s}) = T_{\chi_a 1} + T_{\chi_a 2} + T_{\chi_a 3}, \quad (6c)$$

where

$$T_{\psi_a 1} = \langle [-(\mathbf{V} \cdot \nabla \mathbf{V}_{\psi_a}) \cdot \mathbf{V}_{\psi_s}] \rangle, \quad (7a)$$

$$T_{\psi_a 2} = \left\langle \left(-\omega \frac{\partial \mathbf{V}_{\psi_a}}{\partial p} \cdot \mathbf{V}_{\psi_s} \right) \right\rangle, \quad (7b)$$

$$T_{\psi_a 3} = \langle (-f \mathbf{k} \cdot \nabla \psi_a \times \nabla \psi_s) \rangle, \quad (7c)$$

$$T_{\chi_s 1} = \langle [-(\mathbf{V} \cdot \nabla \mathbf{V}_{\chi_s}) \cdot \mathbf{V}_{\psi_s}] \rangle, \quad (7d)$$

$$T_{\chi_s 2} = \left\langle \left(-\omega \frac{\partial \mathbf{V}_{\chi_s}}{\partial p} \cdot \mathbf{V}_{\psi_s} \right) \right\rangle, \quad (7e)$$

$$T_{\chi_s 3} = \langle (-f \nabla \chi_s \cdot \nabla \psi_s) \rangle, \quad (7f)$$

$$T_{\chi_a 1} = \langle [-(\mathbf{V} \cdot \nabla \mathbf{V}_{\chi_a}) \cdot \mathbf{V}_{\psi_s}] \rangle, \quad (7g)$$

$$T_{\chi_a 2} = \left\langle \left(-\omega \frac{\partial \mathbf{V}_{\chi_a}}{\partial p} \cdot \mathbf{V}_{\psi_s} \right) \right\rangle, \quad (7h)$$

$$T_{\chi_a 3} = \langle (-f \nabla \chi_a \cdot \nabla \psi_s) \rangle. \quad (7i)$$

The terms $T_{\psi_a 1}$, $T_{\chi_s 1}$, and $T_{\chi_a 1}$ represent the conversion rates due to interactions between nonlinear horizontal advections and \mathbf{V}_{ψ_s} . The terms $T_{\psi_a 2}$, $T_{\chi_s 2}$, and $T_{\chi_a 2}$ are the

conversion rates due to interactions between vertical advections and \mathbf{V}_{ψ_s} , and $T_{\psi_a 3}$, $T_{\chi_s 3}$, and $T_{\chi_a 3}$ are the conversion rates due to interactions between the Coriolis parameter and the relative orientations and magnitudes of the two relevant flows.

3. Review of the genesis process of TC Durian (2001)

a. Overview of TC Durian and the simulation results

Tropical Cyclone Durian was generated in the middle of the SCS at 0600 UTC 29 June 2001 as a tropical depression (TD), which developed into a tropical storm (TS) at 0600 UTC 30 June 2001 and then moved northwest. At 1200 UTC 1 July 2001, Durian grew into a typhoon (TY) and then made its first landfall at Zhanjiang in Guangdong province, China, at 1930 UTC 1 July. Durian was a typical tropical cyclone generated in the SCS, which rapidly developed into a typhoon in just 54 h after its genesis and whose minimum sea level pressure and maximum surface wind speed near the TC center reached 970 hPa and 35 m s^{-1} , respectively (see Fig. 1 herein; Zhang et al. 2008b). The genesis location of TC Durian was very close to the Chinese mainland, and it made landfall twice in three days, causing torrential rainfall in most areas of Guangdong, Hainan, and Guangxi provinces of China (Yao 2003; Zhang et al. 2008b; Wang et al. 2010).

Figure 2 shows the comparison between geostationary meteorological satellite images and simulated reflectivity [see also Fig. 7 in Zhang et al. (2008b)]. The embryo of Durian initially evolved from a mesoscale cloud cluster in the north of a MCS (Fig. 2a). After that, the cloud cluster gradually became distinct and tightly organized (Figs. 2c,e). At 1200 UTC 29 June, a well-organized TC vortex had developed (Fig. 2g). The simulated reflectivity also showed a mesoscale convective cloud cluster at 1800 UTC 28 June in the region of $10^{\circ}\text{--}15^{\circ}\text{N}$, $115^{\circ}\text{--}120^{\circ}\text{E}$ (Fig. 2b), and then the cloud north of latitude 15°N gradually enhanced and organized (Figs. 2d,f,h). Meanwhile, a closed low pressure center appeared at 1200 UTC 29 June, corresponding with observations.

b. Characteristics of major systems during TC genesis

As described in section 2, the simulated TC genesis moment (0900 UTC 29 June 2001) was about three hours later than the observed (0600 UTC 29 June 2001), thus, 0900 UTC 29 June 2001 was used as the genesis moment in the following analysis. Figure 3 shows the simulated circulation at the lower level [about 850 hPa, about 1240 m above ground level (AGL)] and midlevel

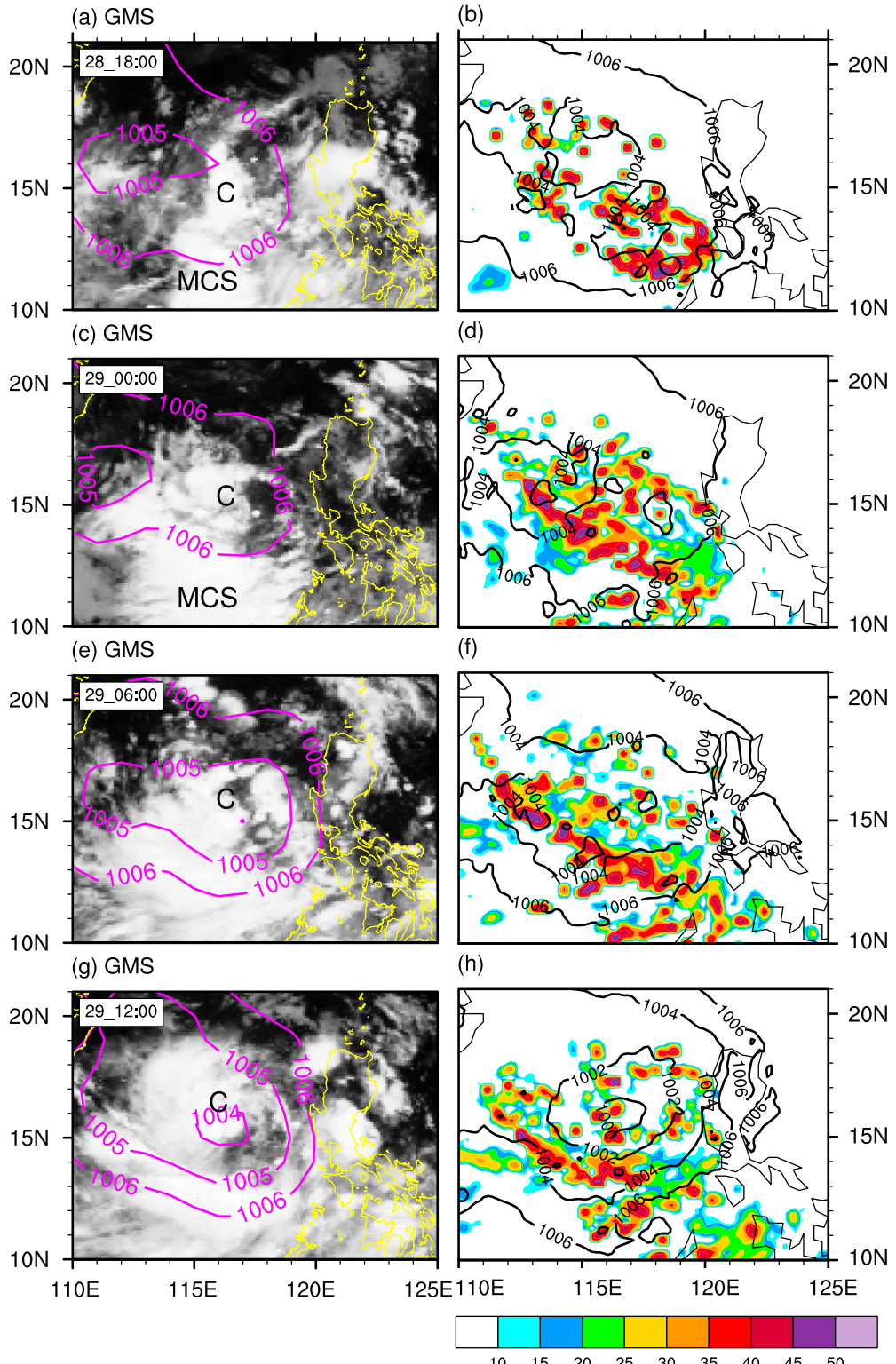


FIG. 2. (a),(c),(e),(g) Geostationary meteorological satellite images and mean sea level pressure (contour, units: hPa) from the National Centers for Environmental Prediction (NCEP) FNL (Final) Operational Global Analysis data on a $1.0^\circ \times 1.0^\circ$ grid. (b),(d),(f),(h) Simulated reflectivity (unit: dBZ) at the midlevel [$\sigma = 0.575$, about 4200 m above ground level (AGL)] and mean sea level pressure (contour, units: hPa). (a),(b) 1800 UTC 28 Jun; (c),(d) 0000 UTC 29 Jun; (e),(f) 0600 UTC 29 Jun 2001; and (g),(h) 1200 UTC 29 Jun. MCS denotes the mesoscale convective system and C denotes the TC-related vortex.

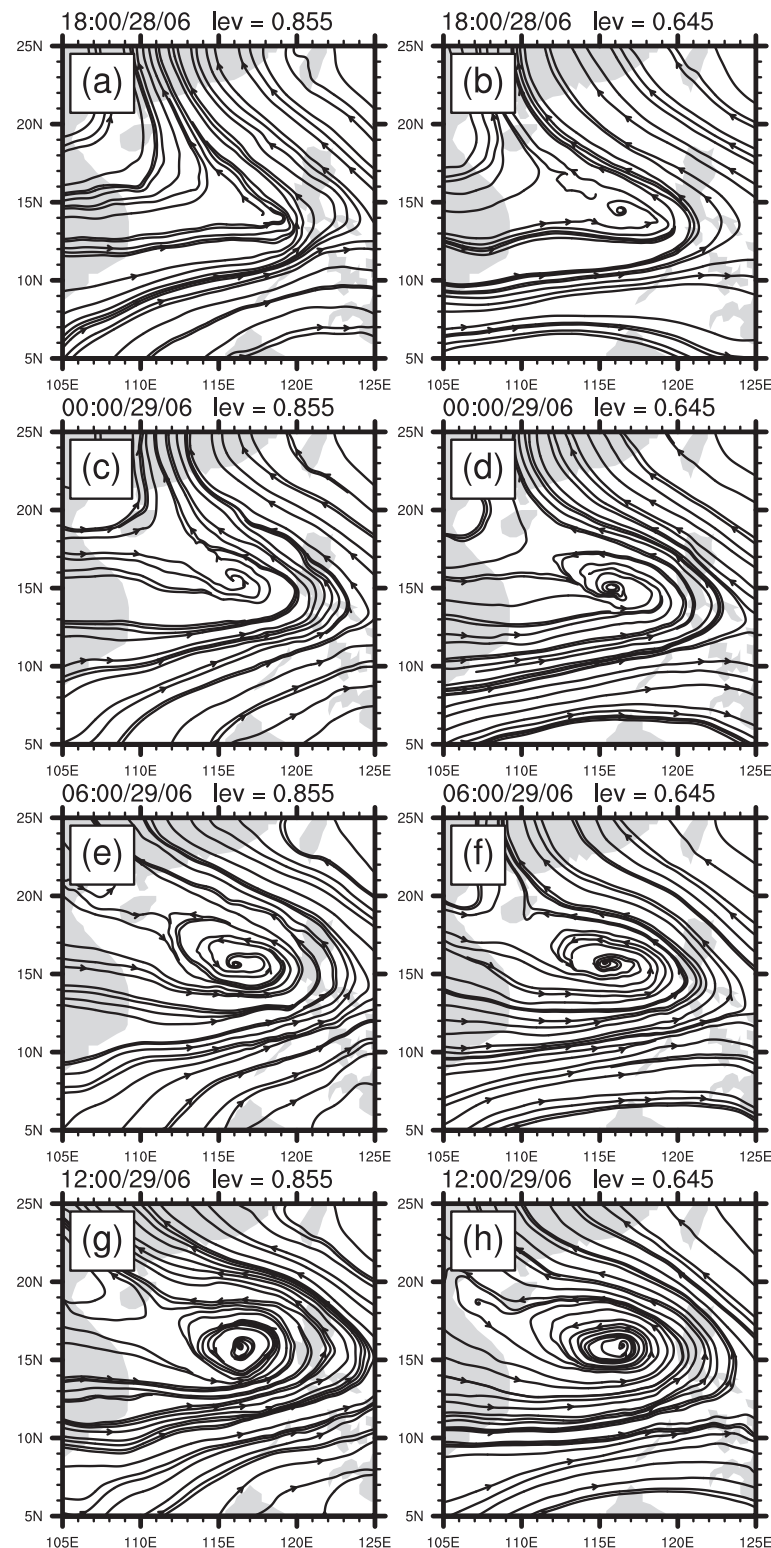


FIG. 3. Simulated streamlines at (a),(c),(e),(g) the lower level ($\sigma = 0.855$, about 1240 m AGL) and (b),(d),(f),(h) the midlevel ($\sigma = 0.645$, about 3360 m AGL) from 1800 UTC 28 Jun to 1200 UTC 29 Jun 2001.

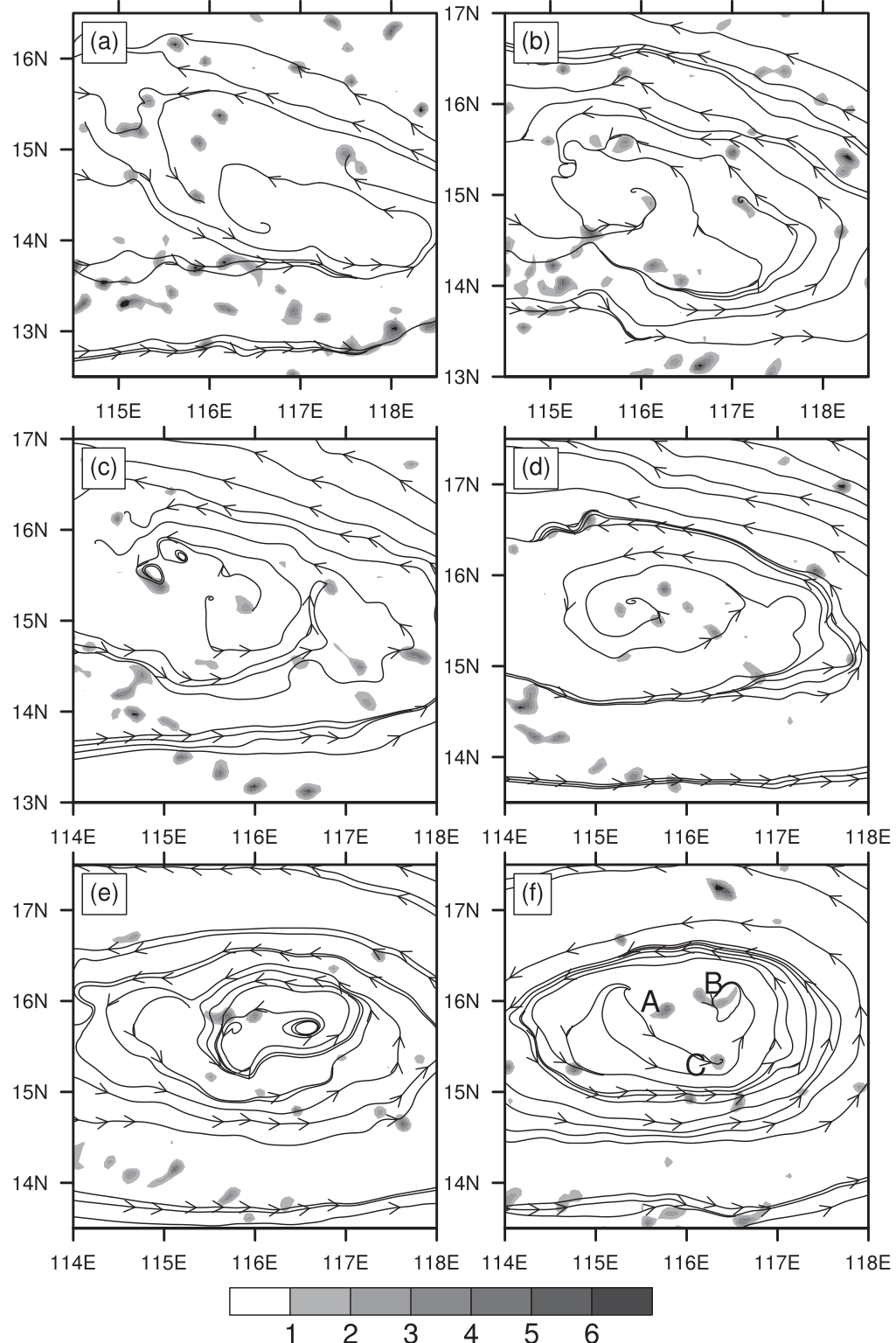


FIG. 4. Circulation (streamline) and VHTs (shaded, $w > 1.0 \text{ m s}^{-1}$) at the midlevel ($\sigma = 0.645$): (a) 2100 UTC 28 Jun, (b) 0000 UTC 29 Jun, (c) 0300 UTC 29 Jun, (d) 0600 UTC 29 Jun, (e) 0900 UTC 29 Jun, and (f) 1200 UTC 29 Jun. Letters "A," "B," and "C" in (f) denote three VHTs.

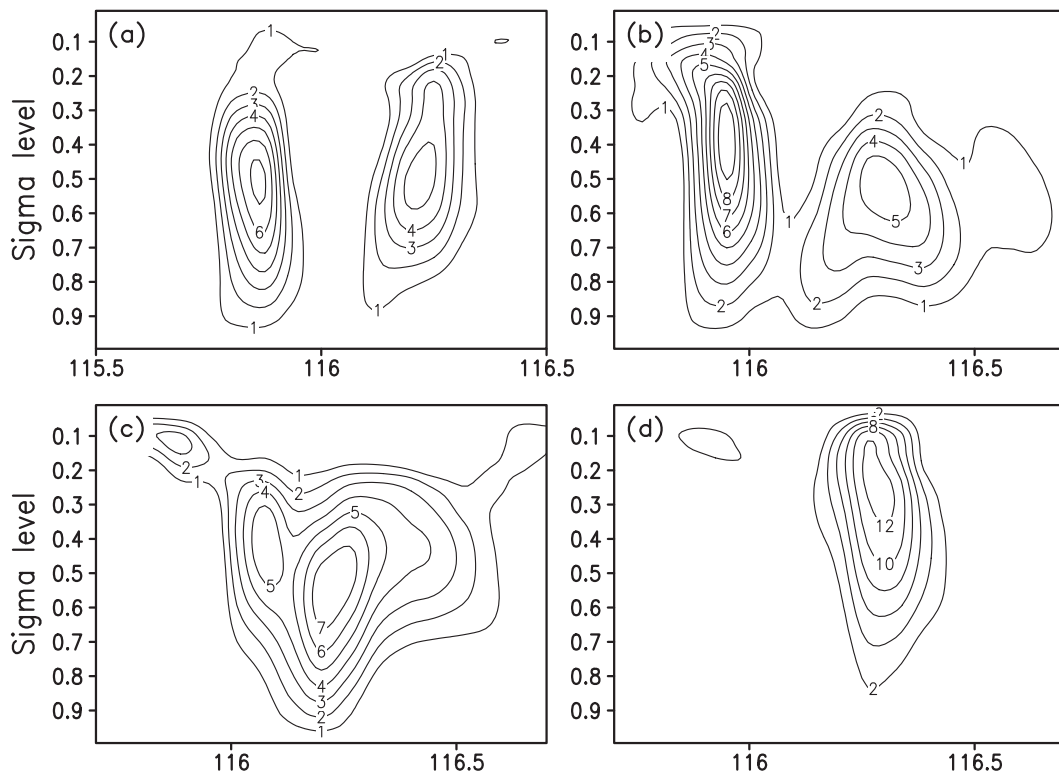


FIG. 5. Cross section of vertical velocity ($\geq 1 \text{ m s}^{-1}$) from $13.6^\circ\text{N}, 115.5^\circ\text{E}$ to $13.9^\circ\text{N}, 116.5^\circ\text{E}$ at (a) 2100 UTC 28 Jun, and from $13.7^\circ\text{N}, 115.5^\circ\text{E}$ to $13.7^\circ\text{N}, 116.5^\circ\text{E}$ at (b) 2120 UTC 28 Jun, (c) 2140 UTC 28 Jun, and (d) 2200 UTC 28 Jun.

(about 650 hPa, about 3360 m AGL) during the genesis process of Durian. It was found that at 1800 UTC 28 June (15 h before the simulated moment of TC genesis; Figs. 3a,b), a typical monsoon trough existed at the lower level, along with an approximately closed weak cyclonic vortex (MCV) at the midlevel in the SCS. At nine hours before the simulated TC genesis (0000 UTC 29 June; Figs. 3c,d), the vortex at the midlevel developed with closed circulation and a cyclonic circulation was also about to develop at the lower level. At three hours before the simulated TC genesis (0600 UTC 29 June), a closed low-level cyclonic vortex formed (Fig. 3e), vertically coupling with the midlevel MCV (Fig. 3f). However, due to the influence of the monsoon trough, both the mid- and low-level vortices were oval at this moment. At three hours after the simulated TC genesis (1200 UTC 29 June; Figs. 3g,h), the vortices at both levels become mostly axisymmetric, particularly at the lower level, indicating the distinct independence of the newborn TC vortex.

Based on the simulation data, Zhang et al. (2010) found that VHTs abundantly occurred from 1800 UTC 28 June to 0200 UTC 29 June within the MCV [Figs. 4 and 13b; see also Fig. 1 in Zhang et al. (2010)]. Then,

VHTs gradually aggregated and merged in the midlevel MCV region after 0600 UTC 29 June (Figs. 4d–f). The number of VHTs also decreased. As an example, Fig. 5 shows that two VHTs at 2100 UTC 28 June 2001 gradually became closer, merged, and grew into a stronger one. At 0900 UTC 29 June, a TC circulation (tropical depression) formed (Fig. 4e). At 1200 UTC 29 June, three major VHTs (denoted by A, B, and C in Fig. 4f) developed and distributed axisymmetrically, along with the aggregation and development of cyclonic vorticity in the lower troposphere. Zhang et al. (2010) suggest that the MCV does not directly pass cyclonic vorticity down to the lower troposphere, but may contribute to the TC genesis in three ways. 1) The MCV-related secondary circulation may enhance VHTs' aggregation, merger, and axisymmetrization. 2) Heat, moisture, and intense vorticity usually accompany strong moist convection in each VHT (Fig. 6), which emerges as the preferred coherent towerlike structure (Montgomery et al. 2006). The MCV helps to reserve the heat, moisture, and vorticity produced by VHTs. 3) Interactions between the MCV, the VHTs, and the low-level vortex contribute to the vertical coupling associated with the TC genesis.

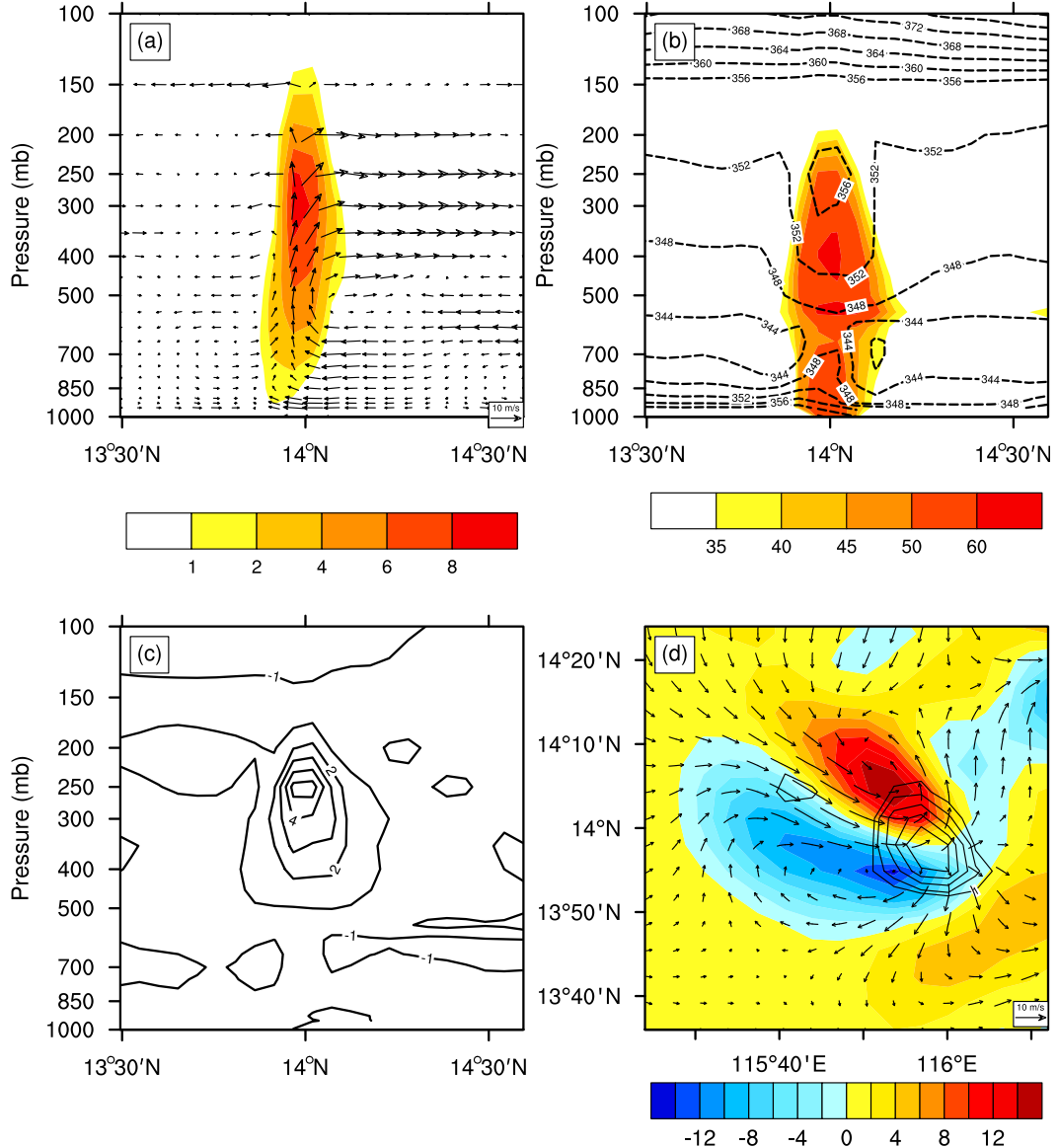


FIG. 6. Cross section of a VHT at longitude of 115.9°E at 1800 UTC 28 Jun. (a) Vertical velocity (shaded, $\geq 1 \text{ m s}^{-1}$), wind vector (v, w) in the plane of the cross section (vector, unit: m s^{-1}). (b) Equivalent potential temperature (contour, unit: K) and reflectivity (shaded, unit: dBZ). (c) Temperature deviation of the VHT with the environment (unit: K). (d) Horizontal distribution of relative vorticity (shaded, unit: 10^{-4} s^{-1}), vertical velocity (contour, $\geq 1 \text{ m s}^{-1}$), and horizontal wind vector at 500 hPa.

The genesis process of Durian consisted of an evolution process from tropical disturbances to a nonaxisymmetric cyclonic circulation and then to an almost-axisymmetric vortex (Fig. 3). Thus, the genesis process was divided into three stages in this study. Stage 1 was the monsoon trough stage (1800 UTC 28 June–0000 UTC 29 June). Stage 2 was the MCV stage (0000–0600 UTC 29 June). Stage 3 was the establishment stage of the TC vortex (0600–1200 UTC 29 June). The KE budgets were analyzed in the

different stages using the above equations and the simulation data.

4. Kinetic energy budget during the TC genesis

a. Kinetic energy of the four flow components

The KEs of the four components from 1800 UTC 28 June to 1200 UTC 29 June 2001 were vertically integrated and averaged in a circular area with a radius of

500 km (Fig. 7). According to the role of the MCV in the TC genesis (Zhang et al. 2010) and the relative position of the MCV to the future TC circulation (Fig. 3), the centers of the area-averaging domains were selected as the cyclonic flow centers of the midlevel MCVs from 1800 UTC 28 June to 0500 UTC 29 June when the midlevel MCV was developing and the low-level cyclonic vortex had not yet formed. Then the centers were selected as the cyclonic flow centers of the low-level vortices from 0600 to 1200 UTC 29 June, when a discernable closed near-surface vortex, and later the tropical depression, had developed (Table 1). It is apparent (Fig. 7) that the KE of the SRF (K_{ψ_s}) was much larger than that of the other three KEs and kept on growing throughout the whole genesis period. A distinct growth rate was particularly observed after 0000 UTC 29 June, when the midlevel MCV developed rapidly and a low-level cyclonic circulation developed later (Fig. 3), indicating that the symmetric rotational motion strengthened rapidly. The KEs of the divergent flow components were smaller than those of the rotational flow components and the KE of the SDF was the smallest. The genesis process of TC Durian was essentially dominated by the SRF. Terms K_{ψ_a} and K_{χ_a} were almost unchanged with time, while K_{χ_s} initially increased and then started to decrease at about 2300 UTC 28 June, followed by a rapid increase of K_{ψ_s} .

b. Kinetic energy budgets of the four flow components

Sources and sinks of the KEs of the four components in the aforementioned three stages are presented in Fig. 8. The interaction terms [R in Eqs. (1a)–(1d)] between the different flow components were omitted in the following analysis, as they are much smaller than the other terms. The most distinct variations (tendencies) in the KEs were from the SRF (Figs. 8a–c), which was consistent with the above analysis (Fig. 7). Furthermore, most of the variations were restricted at the mid- and lower levels, consistent with the fact that the midlevel MCV and the low-level TC vortex are major systems during these three stages (Fig. 3). The increase of K_{ψ_s} in Fig. 7 is mainly due to the KE conversion term C_{ψ_s} , which is partially consumed by the residual term D_{ψ_s} at the lower and midlevels, implying the possible roles of friction dissipation and subgrid-scale processes. Furthermore, the energy flux divergence term F_{ψ_s} acted as a source at the mid- and higher levels and as a weak sink at the lower levels, implying the effects of vertical transfer of the KE. The potential energy term P_{ψ_s} was always about zero, indicating that little potential energy was directly transformed to K_{ψ_s} . The conversion term associated with K_{χ_s} (red lines in Figs. 8g–i) showed a similar magnitude and vertical distribution to those associated

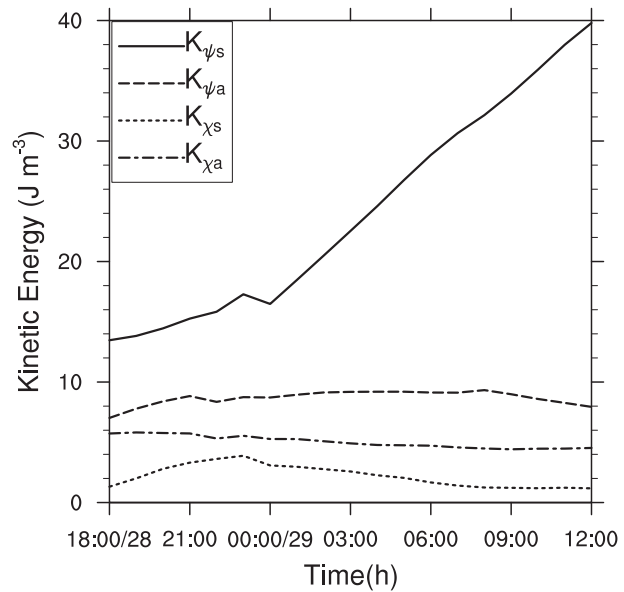


FIG. 7. Temporal evolution of vertically integrated and area-averaged (in a 500-km-radius domain centered by points listed in Table 1) KEs of the SRF (K_{ψ_s}), ARF (K_{ψ_a}), SDF (K_{χ_s}), and ADF (K_{χ_a}) from 1800 UTC 28 Jun to 1200 UTC 29 Jun. Unit: J m^{-3} .

with K_{ψ_s} (red lines in Figs. 8a–c) at the mid- and lower levels. The conversion term associated with the ADF (C_{χ_a}) may have also partially contributed to the increase of the KEs of the rotational flow components (K_{ψ_s} and K_{ψ_a}) (red lines in Figs. 8j–l). Compared with stage 1, the midlevel K_{ψ_s} substantially increased in stage 2. This increase of symmetric circulation in stage 2 mainly occurred at the midlevel rather than at the low level, indicating that the midlevel MCV was quickly developing at this stage while the low-level circulation continuously increased in strength. The low-level K_{ψ_s} also sharply increased, particularly in stage 3, representing the establishment of the TC vortex.

From the aspect of systems development, a moderate increase in the KE of the SRF took place in the region of the monsoon trough in stage 1 (Fig. 8a), during which there were a large number of VHTs occurring and developing within the midlevel MCV

TABLE 1. Center points from 1800 UTC 28 Jun to 1200 UTC 29 Jun 2001. The points were selected as the cyclonic flow centers of the midlevel MCVs from 1800 UTC 28 Jun to 0500 UTC 29 Jun 2001, and as the cyclonic flow centers of the low-level vortices from 0600 to 1200 UTC 29 Jun 2001.

Time	Center
1800–2100 UTC 28 Jun	(14.5°N, 115.8°E)
2200–2300 UTC 28 Jun	(15.0°N, 115.8°E)
0000–0700 UTC 29 Jun	(15.8°N, 115.8°E)
0800–1200 UTC 29 Jun	(15.8°N, 116.8°E)

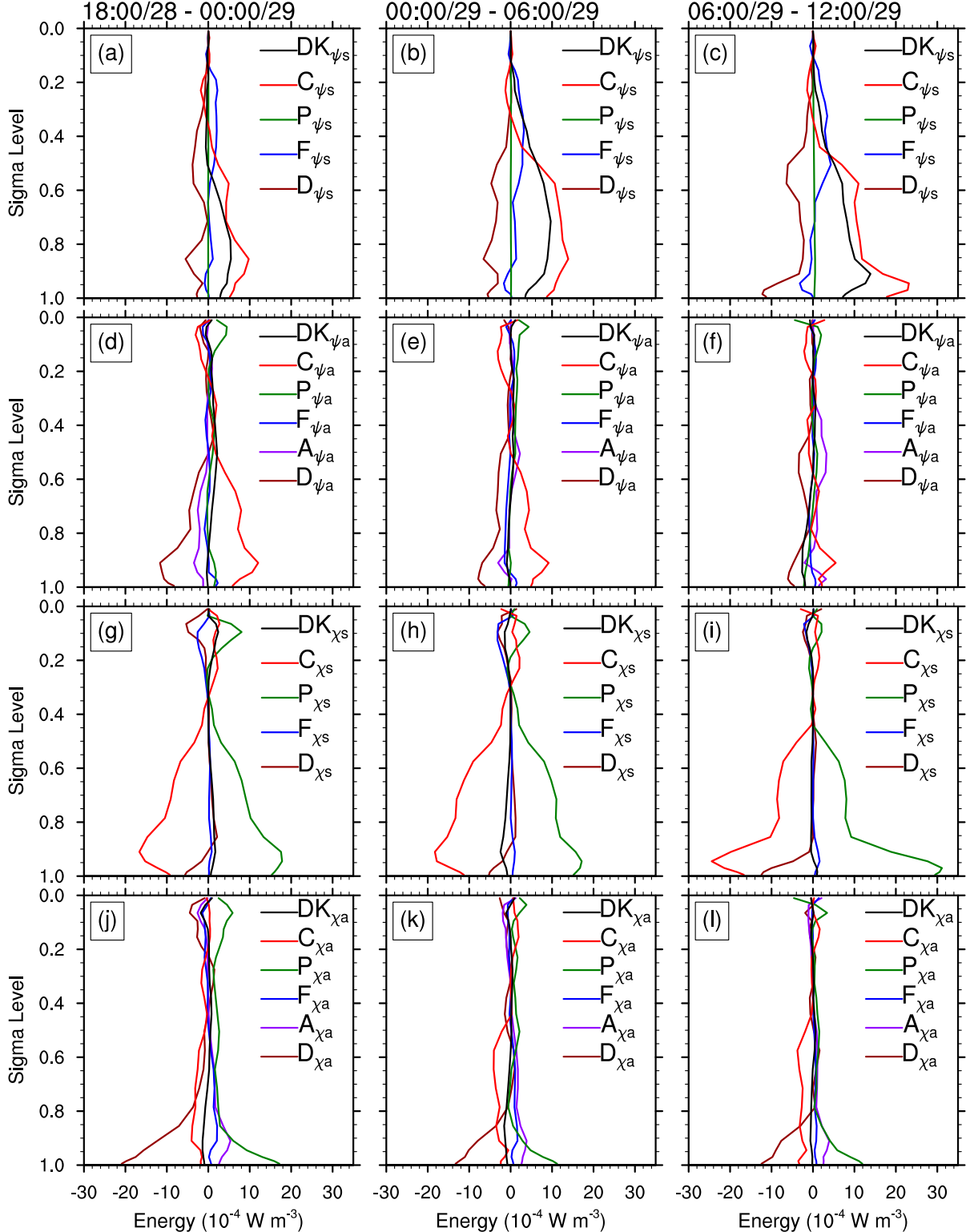


FIG. 8. Vertical profiles of source and sink terms associated with the KE budgets of the SRF (K_{ψ_s}), ARF (K_{ψ_a}), SDF (K_{χ_s}), and ADF (K_{χ_a}) averaged in a 500-km-radius domain centered by points listed in Table 1 and in the three stages: (a),(d),(g),(j) 1800 UTC 28 Jun–0000 UTC 29 Jun; (b),(e),(h),(k) 0000–0600 UTC 29 Jun; and (c),(f),(i),(l) 0600–1200 UTC 29 Jun 2001. Unit: 10^{-4} W m^{-3} .

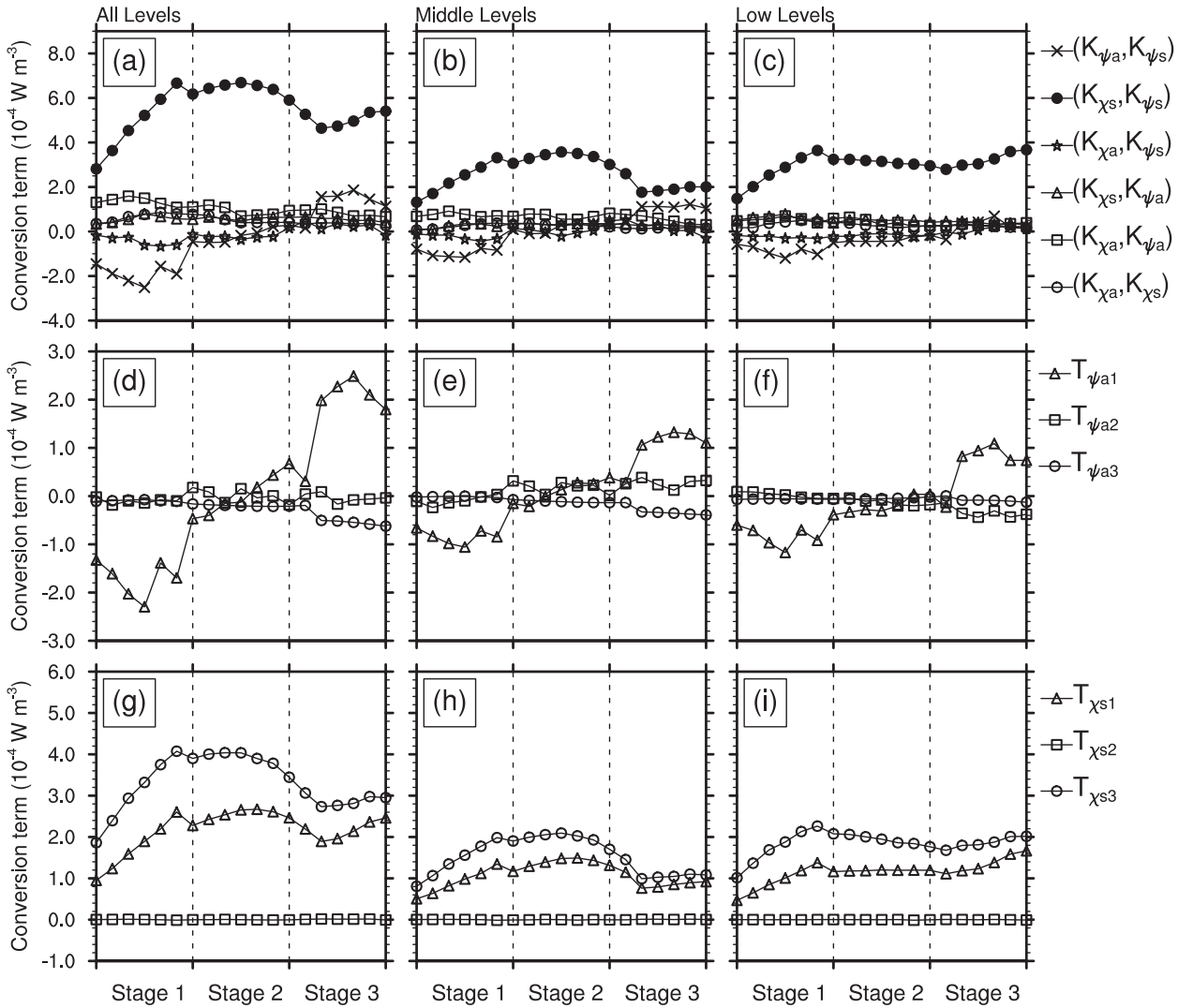


FIG. 9. Temporal evolution of vertically integrated and area-averaged (in a 500-km-radius domain centered by points listed in Table 1) KE conversion terms through (a),(d),(g) all levels ($\sigma = 0.995\text{--}0.01$, about 40–18 000 m AGL), (b),(e),(h) midlevels ($\sigma = 0.785\text{--}0.44$, about 1900–6000 m AGL), and (c),(f),(i) low levels ($\sigma = 0.995\text{--}0.855$, about 40–1240 m AGL). (a)–(c) KE conversion terms between the four wind components. (d)–(f) The three components of (K_{ψ_a}, K_{ψ_s}) . (g)–(i) The three components of (K_{χ_s}, K_{ψ_s}) . Unit: 10^{-4} W m^{-3} .

region [Zhang et al. (2010), also see Fig. 4c]. In stage 2 (Fig. 8b), the developed midlevel MCV (Fig. 4d) maintained a more favorable environment for VHTs and their interaction enhanced the KE of the SRF in this stage (Fig. 8b). It is notable that the KE of the SRF at the surface in stages 1 and 2 did not show as rapid an increase as those at the mid- and lower levels (Figs. 8a,b), which may be related to the fact that the surface TC circulation had not been set up in these two stages. In stage 3 (Fig. 8c), the KE of the SRF continued to increase at the midlevel and began to increase more rapidly at the surface, as the surface TC vortex established at the lower level and vertically coupled with the preexisting midlevel MCV circulation in this stage.

It was found that the relatively rapid increase of the conversion term, C_{ψ_s} , at the midlevel can explain the growth of DK_{ψ_s} at stage 2, which was partially offset by a slight increase of the magnitude of D_{ψ_s} at both the mid- and lower levels. In stage 3, most of the increase in K_{ψ_s} (Fig. 8) was caused by the sustained large magnitude of C_{ψ_s} at the midlevel since stage 2 and the rapid increase of C_{ψ_s} at the lower level, which was largely offset by the distinct increase of the magnitude of D_{ψ_s} at the lower level. Moreover, C_{ψ_s} at stage 2 was mainly contributed by the increase of (K_{χ_s}, K_{ψ_s}) and (K_{ψ_a}, K_{ψ_s}) at both the low and midlevels (Figs. 9a–c). At stage 3, the contributing term (K_{χ_s}, K_{ψ_s}) became weak at the midlevel and grew strong at the low level. The term (K_{χ_s}, K_{ψ_s}) was

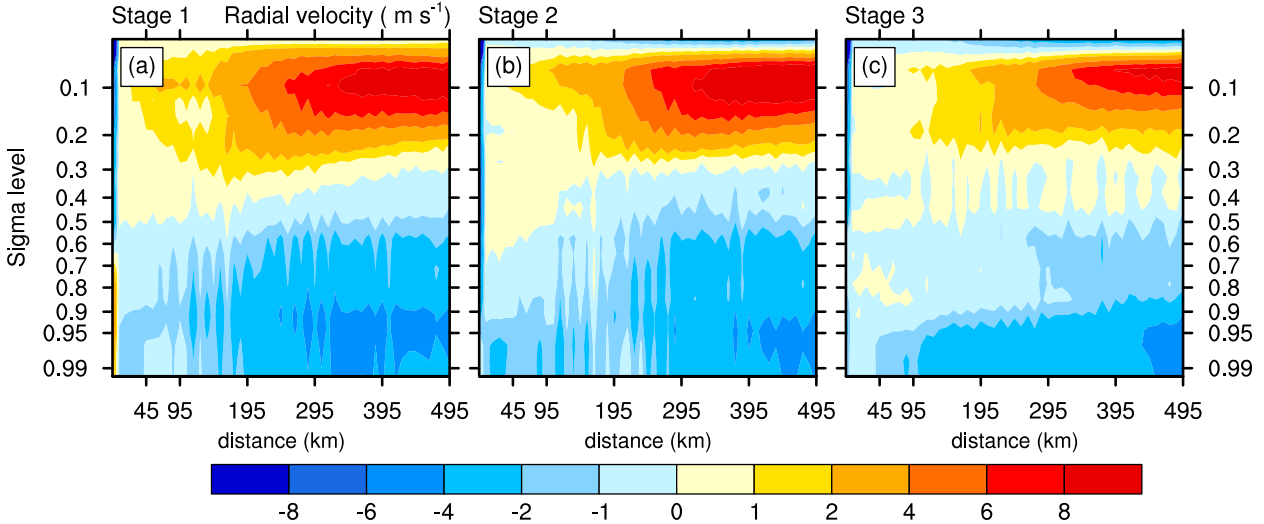


FIG. 10. Height–radius cross sections of azimuthally averaged radial velocity (unit: m s^{-1}) in (a) stage 1, (b) stage 2, and (c) stage 3.

dominated by $T_{\chi_s 1}$ and $T_{\chi_s 3}$ [Eqs. (7d) and (7f)] at both the mid- and low levels (Figs. 9g–i), where $T_{\chi_s 1}$ represents the conversion rate determined by the interaction between the symmetric rotational circulation (\mathbf{V}_{ψ_s}) and the horizontal advection of the symmetric divergent circulation (\mathbf{V}_{χ_s}), similar to the results in Carr and Williams (1989) and Li and Wang (1994). The term $T_{\chi_s 3}$ was due to the interaction between the Coriolis parameter and the relative orientations and magnitudes of the SRF (\mathbf{V}_{ψ_s}) and the SDF (\mathbf{V}_{χ_s}). The decrease in $T_{\chi_s 3}$ in stage 3 mainly occurred in the middle troposphere (Figs. 9a–c). Figure 10 shows the height–radius cross sections of azimuthally averaged radial velocities in the three stages. Intense inward radial motions dominated the mid- and lower levels in stages 1 and 2 and then the inward radial motions at the midlevel decreased noticeably in stage 3, which may have contributed to the decrease of (K_{χ_s}, K_{ψ_s}) at the midlevel (Fig. 9b).

As for the other three KEs, the KE tendencies were not as large as that of the SRF, but they did play a role in the increase of the KE of the SRF and contributed to the establishment of the TC circulation through the conversion terms between the different KEs (Fig. 8). Among them, K_{χ_s} was the main and direct contributor. The KE conversions from the available potential energy by pressure gradient force terms (P_{χ_s}, P_{χ_a}) due to the flows crossing isobaric lines to the low pressure area were the most important sources of K_{χ_s} and K_{χ_a} , which were largely balanced out by the conversion terms (C_{χ_s} and C_{χ_a}) at the mid- and lower levels and residual terms (D_{χ_s} and D_{χ_a}) near the surface. Moreover, the slight increase in C_{χ_s} at the midlevel in stage 2 and the distinct increase of C_{χ_s} at the lower level in stage 3 may have

been partially due to the convergence effect of the MCV and the surface TC vortex, respectively.

c. Major source terms contributing to K_{ψ_s}

Based on the KE budget, it can be seen that K_{χ_s} was mainly transformed from potential energy (P_{χ_s}), which was regarded as the positive feedback between reduced central pressure and convergent flow according to Eq. (1c). Figure 11 summarizes the frequency of the vertical velocity and diabatic heating within the storm-centered domain with a radius of 200 km, to explore the relationship between small-scale convection and the diabatic heating rate. The diabatic heating rate was calculated using the residual of the θ field in space and time, that is, $\dot{\theta} = \partial\theta/\partial t + \mathbf{v} \cdot \nabla\theta$ (Hendricks et al. 2004). It can be seen that the maximum velocity was located at the midlevel in stages 1 and 2 (Figs. 11a,b), then gradually went down to the low level and became weak in stage 3 (Fig. 11c). The diabatic heating also showed similar variation and distribution as the vertical velocity (Figs. 11d–f). It can be inferred that small-scale convection, including VHTs, is crucial to the collection and transfer of thermal energy. Based on the aforementioned genesis process, at stages 1 and 2, abundant disorganized-small-scale convection or VHTs occurred associated with the release of latent heat. Thus, the air column at both the low and midlevels was heated as well as the potential energy growing. Furthermore, compared with stage 1, the vertically accumulated temperature anomaly increased distinctly at stage 2 (Fig. 12b), which helped to enhance the potential energy. In contrast to stages 1 and 2, both the number and intensity of convection generally decreased at stage 3 (Figs. 11c

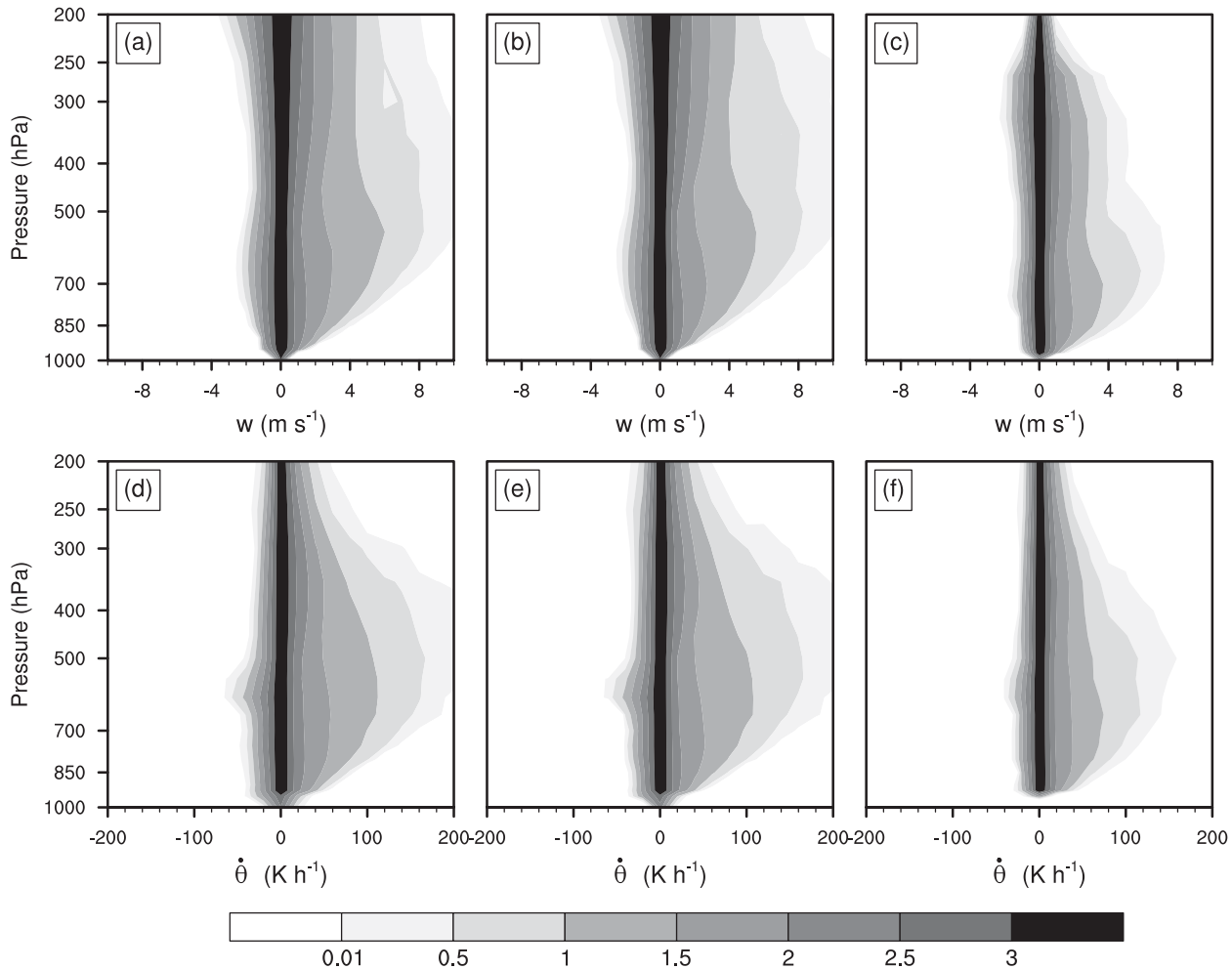


FIG. 11. Contoured frequency by altitude diagrams (CFADs) for (top) vertical velocity and (bottom) diabatic heating of (a), (d) stage 1; (b), (e) stage 2; and (c), (f) stage 3.

and 13b) and latent heating at the midlevel became weaker. However, convection at this stage organized within the initial TC vortex, benefiting the concentration of latent heat. So the temperature anomaly still increased at the low and midlevels. Though the midlevel radial inward motion decreased at stage 3, the low-level radial velocity increased (Fig. 10). Thus, the term P_{χ_s} still increased due to the accumulated pressure gradient at the lower level. Then, K_{χ_s} transformed from term P_{χ_s} was largely converted to K_{ψ_s} .

Here (K_{ψ_a}, K_{ψ_s}) was another important KE conversion term during the TC genesis, which was negative in stage 1, close to zero in stage 2, and positive in stage 3 (Figs. 9d–f), indicating that in stage 1 when the monsoon trough was the main dominating system, there was a distinct KE conversion from the SRF to the ARF and then the conversion reversed with the establishment of the TC vortex. The term (K_{ψ_a}, K_{ψ_s}) was mainly

contributed by $T_{\psi_a 1}$ [Eq. (7a), Figs. 9d–f], which changed from a sink of K_{ψ_s} in stage 1 to a source of K_{ψ_s} in stage 3. The term $T_{\psi_a 1}$ was determined by the interaction between the symmetric rotational circulation and the horizontal advection of the asymmetric rotational circulation. The negative (K_{ψ_a}, K_{ψ_s}) dominated the midlevel in stages 1 and 2 (Fig. 13a) when VHTs emerged abundantly (Fig. 13b) in the MCV region (a 300-km-radius circular area around the center points in Table 1). Then the positive (K_{ψ_a}, K_{ψ_s}) enhanced significantly at the lower level from stage 2 and at the midlevel from stage 3 (Fig. 13a) when the number of VHTs decreased distinctly (Fig. 13b). There may be some relations between VHTs and the KE conversion of (K_{ψ_a}, K_{ψ_s}) . The horizontal distributions of (K_{ψ_a}, K_{ψ_s}) and VHTs at the lower, mid-, and upper levels in the above 300-km-radius area also supported the above hypothesis (Fig. 14), which still needs more proof in future work. There were

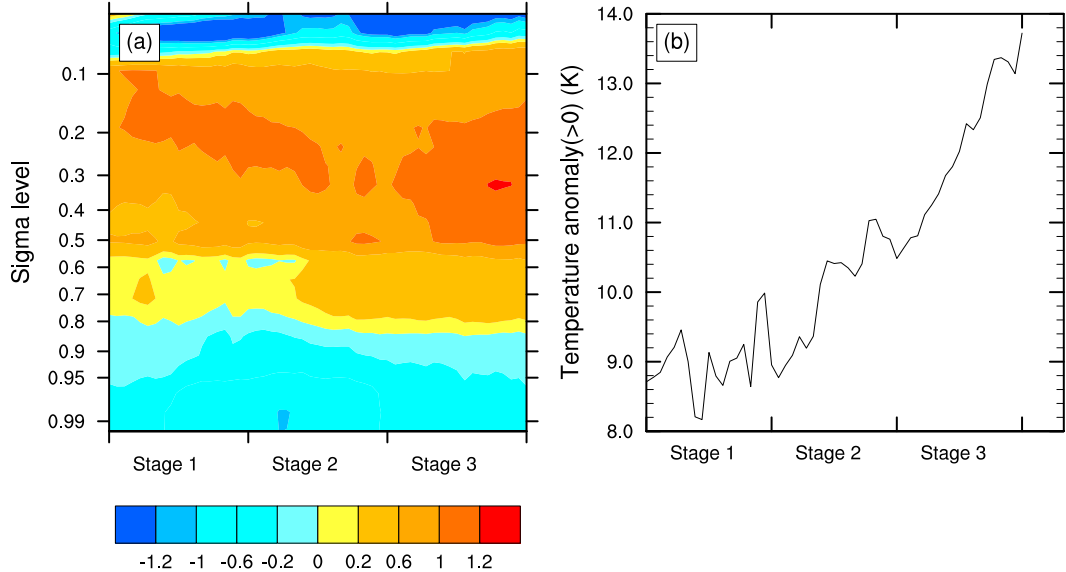


FIG. 12. (a) Height-time cross section of area-averaged (in a 300-km-radius domain centered by points listed in Table 1) temperature anomaly (unit: K). (b) Vertically cumulative positive temperature anomaly (unit: K).

more VHTs at the mid- and upper levels than the lower level (Figs. 13b and 14). Furthermore, VHTs emerged abundantly in stage 1 and then the number of VHTs reduced distinctly in stages 2 and 3 because of aggregation and merger (Zhang et al. 2010).

The flux divergence term (F_{ψ_s}), though not as crucial as the conversion terms [(K_{χ_s}, K_{ψ_s}) , (K_{ψ_a}, K_{ψ_s})], was another important contributor to the vertical distribution

of the KE budget of the SRF (Figs. 8a–c). The height-time cross sections of F_{ψ_s} and its two simplified components [Eq. (1a)], the horizontal advection term ($-\mathbf{V} \cdot \nabla K_{\psi_s}$) and the vertical advection term ($-\omega \partial K_{\psi_s} / \partial p$), are presented in Fig. 15. The distribution and variation of F_{ψ_s} were mainly dominated by the vertical advection term (Figs. 15a,c). The F_{ψ_s} at the lower levels was mainly negative with positive F_{ψ_s} located above. In stages 2

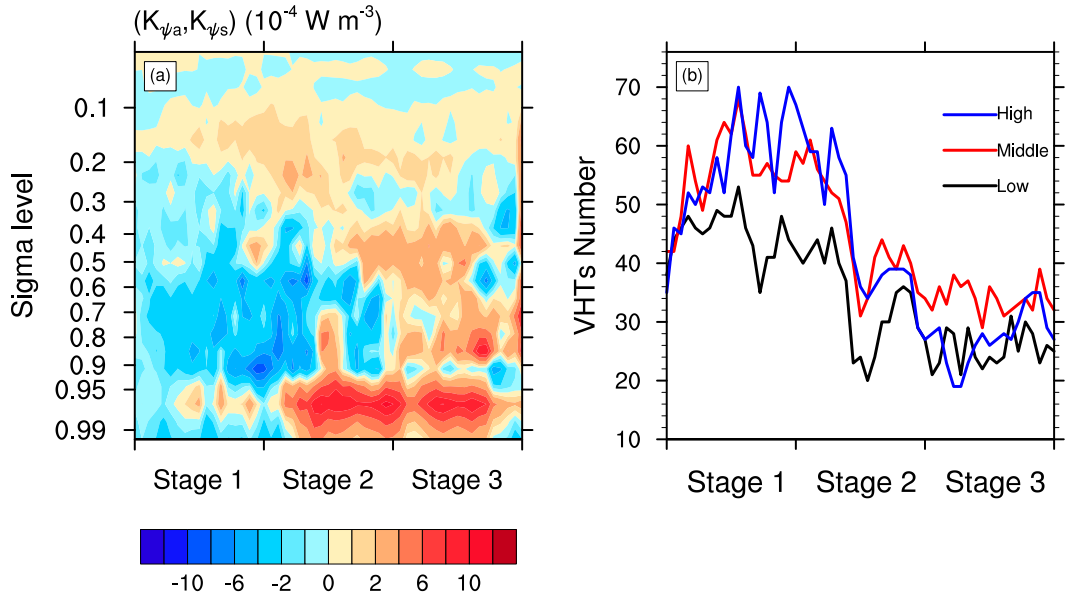


FIG. 13. (a) Height-time cross sections of area-averaged (in a 300-km-radius domain centered by points listed in Table 1) conversion term (K_{ψ_a}, K_{ψ_s}) (unit: 10^{-4} W m^{-3}). (b) Temporal evolution of VHT numbers in the above 300-km-radius area at the lower ($\sigma = 0.855$, about 1240 m AGL), mid- ($\sigma = 0.645$, about 3360 m AGL), and upper ($\sigma = 0.325$, about 7900 m AGL) levels.

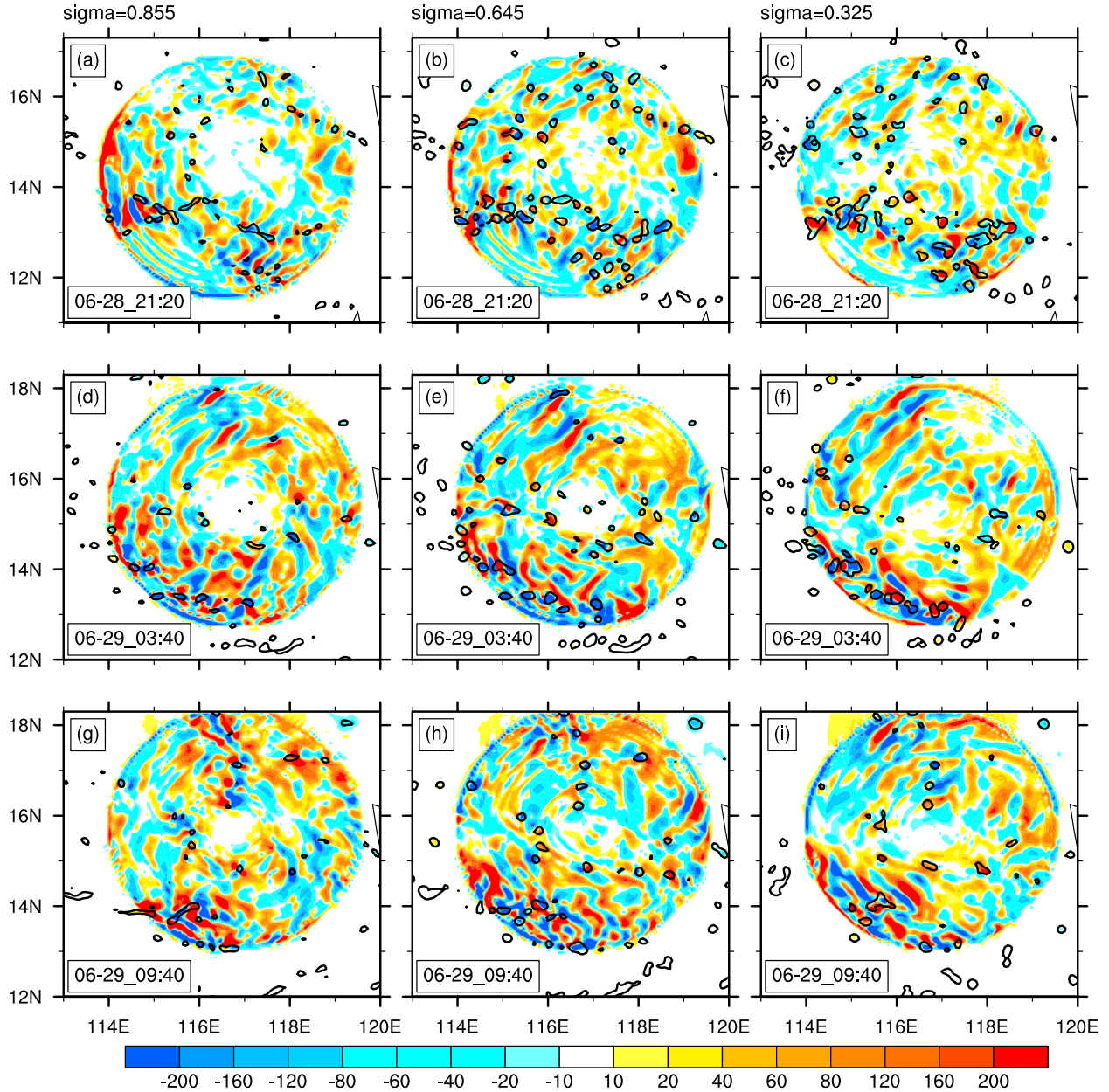


FIG. 14. The KE conversion term (K_{ψ_a} , K_{ψ_s}) (shaded, unit: $10^{-4} \text{ W kg}^{-1}$) and VHTs (contour, identified by vertical upward velocity $> 1 \text{ m s}^{-1}$) at the (a),(d),(g) lower ($\sigma = 0.855$, about 1240 m AGL); (b),(e),(h) mid- ($\sigma = 0.645$, about 3360 m AGL); and (c),(f),(i) upper ($\sigma = 0.325$, about 7900 m AGL) levels at (a)–(c) 2120 UTC 28 Jun; (d)–(f) 0340 UTC 29 Jun; and (g)–(i) 0940 UTC 29 Jun.

and 3, the magnitudes of the positive F_{ψ_a} at the upper levels and the negative F_{ψ_s} at the lower levels enhanced significantly, especially in stage 3 when the TC vortex developed and distinctly enhanced the vertical transportation of F_{ψ_s} (Fig. 8c).

d. Quantified summary of KE budget terms

Vertically integrated and area-averaged KE budgets of the four flow components are shown in Figs. 16, 17,

and 18. In all the three stages, the KEs of the SRF always possessed the largest tendencies among the four components vertically integrated through all the levels (Fig. 16), the midlevels (Fig. 17), and the lower levels (Fig. 18). Furthermore, they always increased ($DK_{\psi_s} > 0$) and grew much faster in the final two stages when the MCV and the TC vortex developed, indicating a distinct axisymmetrization process during the TC genesis (Figs. 16–18). Comparing DK_{ψ_s} at the midlevels with

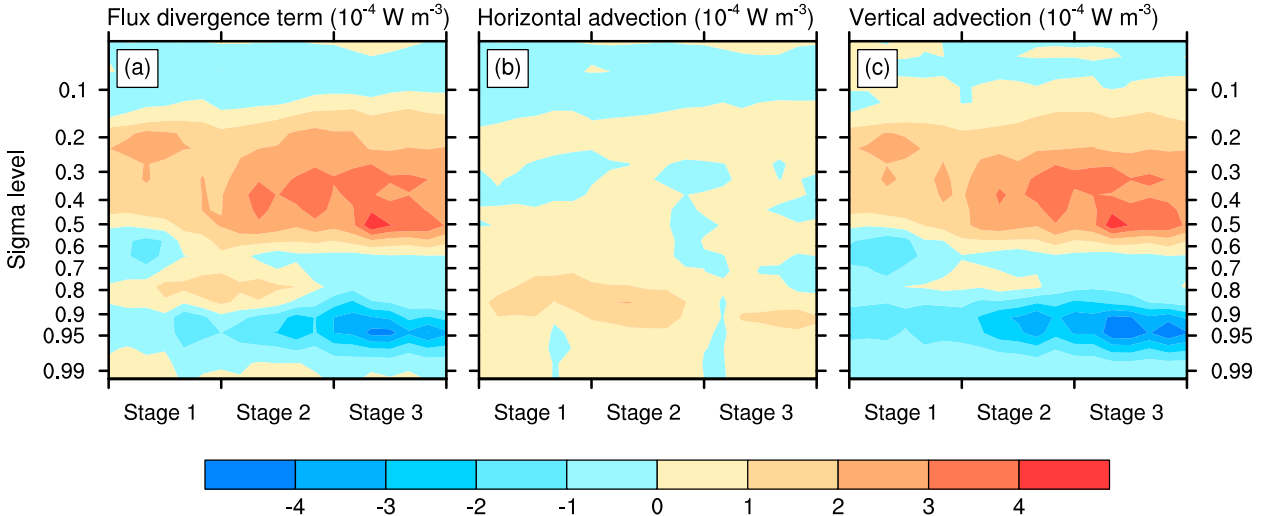


FIG. 15. (a)–(c) Height–time cross sections of area-averaged (in a 500-km-radius domain centered by points listed in Table 1) (a) flux divergence term (F_{ψ_s}) in the equation of KE tendency of the SRF, (b) horizontal advection component of F_{ψ_s} , and (c) vertical advection component of F_{ψ_s} . Unit: 10^{-4} W m^{-3} .

that at the lower levels (Figs. 17 and 18), it is notable that DK_{ψ_s} in stage 2 ($4.02 \times 10^{-4} \text{ W m}^{-3}$; Fig. 16b) was largely contributed by DK_{ψ_s} at the midlevels ($2.03 \times 10^{-4} \text{ W m}^{-3}$; Fig. 17b), which implies an important contribution of the MCV. The term DK_{ψ_s} in stage 3 ($4.68 \times 10^{-4} \text{ W m}^{-3}$; Fig. 16c) was largely contributed by DK_{ψ_s} at the lower levels ($2.65 \times 10^{-4} \text{ W m}^{-3}$; Fig. 18c), which implies an important role of the surface TC vortex. Moreover, the KE conversion term, (K_{χ_s}, K_{ψ_s}) , was the main contributor to DK_{ψ_s} , which was partially consumed by (K_{ψ_a}, K_{ψ_s}) in stage 1 (Figs. 16a, 17a, and 18a) and by D_{ψ_s} in all three stages (Figs. 16–18). The term (K_{ψ_a}, K_{ψ_s}) gradually reversed from a sink of K_{ψ_s} in stage 1 to a weak source of K_{ψ_s} in stage 3 (Figs. 16–18), which was consistent with the above analysis. The term P_{χ_s} was the main contributor to K_{χ_s} , and was mainly consumed by (K_{χ_s}, K_{ψ_s}) and partially consumed by D_{χ_s} (Figs. 16–18). For the KEs of the divergent flows, the baroclinic processes (P_{χ_s}, P_{χ_a}) were the major sources, while the KE conversions to rotational flows and energy dissipation (D_{χ_s}, D_{χ_a}) were the major sinks, particularly at the lower levels. In general, little available potential energy (APE) directly transformed to the KE of the SRF. In contrast, the APE transformed to the KE of the SDF at first, and then the KE of the SDF further converted to the KE of the SRF during TC genesis, which is consistent with the work of Ding and Liu (1985b) on energy conversion during a TC's development and intensification process.

e. Schematic summary and discussion

A schematic of the energy budget during TC Durian's genesis process is presented in Fig. 19. The genesis

(axisymmetrization) process of TC Durian was dominated by the SRF, which possessed the largest KE and was always strengthening in all three stages of the TC genesis (denoted by the horizontal empty arrow in the middle of Fig. 19). From the aspect of KE, the increase in the SRF was directly contributed from the SDF or inward radial flow, and was also impaired by friction and the subgrid effect (denoted by the upper two empty arrows in Fig. 19). Furthermore, it can be seen that the SDF was largely converted from potential energy through baroclinic processes (P_{χ_s} , denoted by left filled arrows in Fig. 19). According to the budget theory of APE, latent heating can impact the variation in APE (Ding and Liu 1985b; Fu et al. 2011). In this case, VHTs emerged abundantly in stages 1 and 2 in the favorable environment provided by the MCV and intense upward motions of moist air associated with VHTs released massive latent heat. The heat and vorticity produced by VHTs was maintained for a while rather than quickly diluted by the surroundings. Then the VHT-generated heat and vorticity was reserved within the MCV, warming the air column and benefitting the accumulation of APE and the transformation from APE to KE of the SDF. Compared with stage 1, the KE of the low- to midlevel circulation increased, especially at the midlevel in stage 2, representing the rapid development of the MCV. Impacted by the secondary circulation of MCV, more VHTs aggregated or merged within the MCV region. In stage 3, both the intensity of VHTs and the latent heating rate decreased. However, VHTs started to organize. So after the genesis, VHT-generated heat can be trapped within the surface TC vortex and MCV. As a

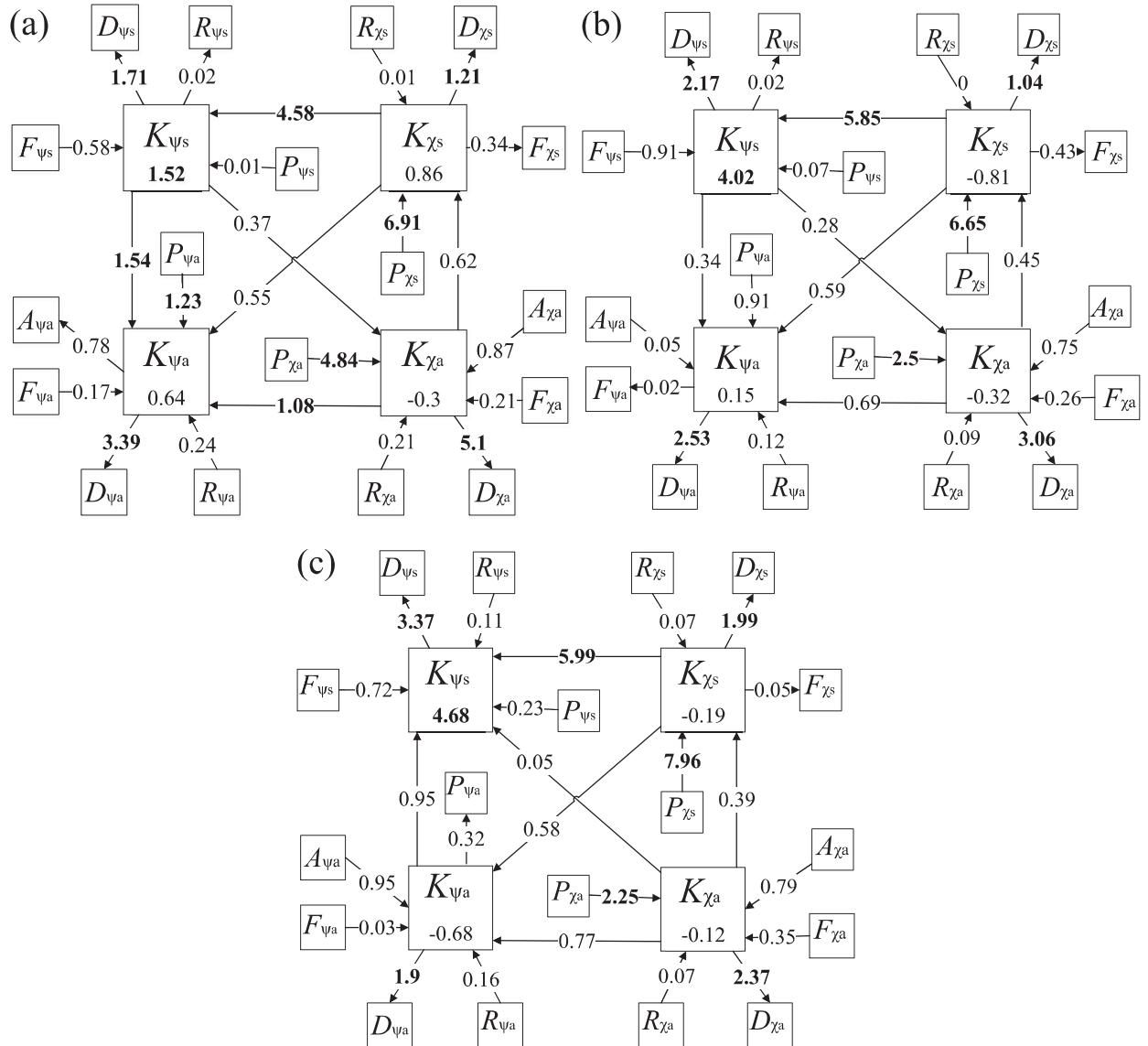


FIG. 16. Vertically integrated and area-averaged (in a 500-km-radius domain centered by points listed in Table 1) KE budgets of the four wind components through all levels ($\sigma = 0.995\text{--}0.01$, about 40–18 000 m AGL) in the three stages, units: 10^{-4} W m^{-3} . (a) 1800 UTC 28 Jun–0000 UTC 29 Jun; (b) 0000–0600 UTC 29 Jun; and (c) 0600–1200 UTC 29 Jun. Boldface numbers show the absolute values larger than 1.

result, potential energy accumulates. Owing to the decrease (increase) of inward radial wind at the mid-(lower) level, KE increased more significantly near the surface than at the midlevel.

During the whole TC genesis process, positive temperature anomalies dominated the mid- and upper levels, the center of which gradually extended downward (Fig. 12), suggesting continuous warming of the atmospheric column and the contributions of the VHTs in stages 1 and 2 and more organized convection associated with the TC vortex in stage 3 to the maintenance

of the positive temperature anomalies. Though the lifetime of a VHT is very short (around one hour; Hendricks et al. 2004; Montgomery et al. 2006), the latent heat, moisture, and vorticity associated with the VHT may be still reserved in the MCV region or TC vortex for a while after the VHT starts decaying, which in turn benefits the maintenance of the above positive temperature anomalies and, furthermore, the accumulation and release of APE (Zhang et al. 2010). In stage 3, a TC vortex with a low central pressure and a warm core (Fig. 12) was gradually set up, during which

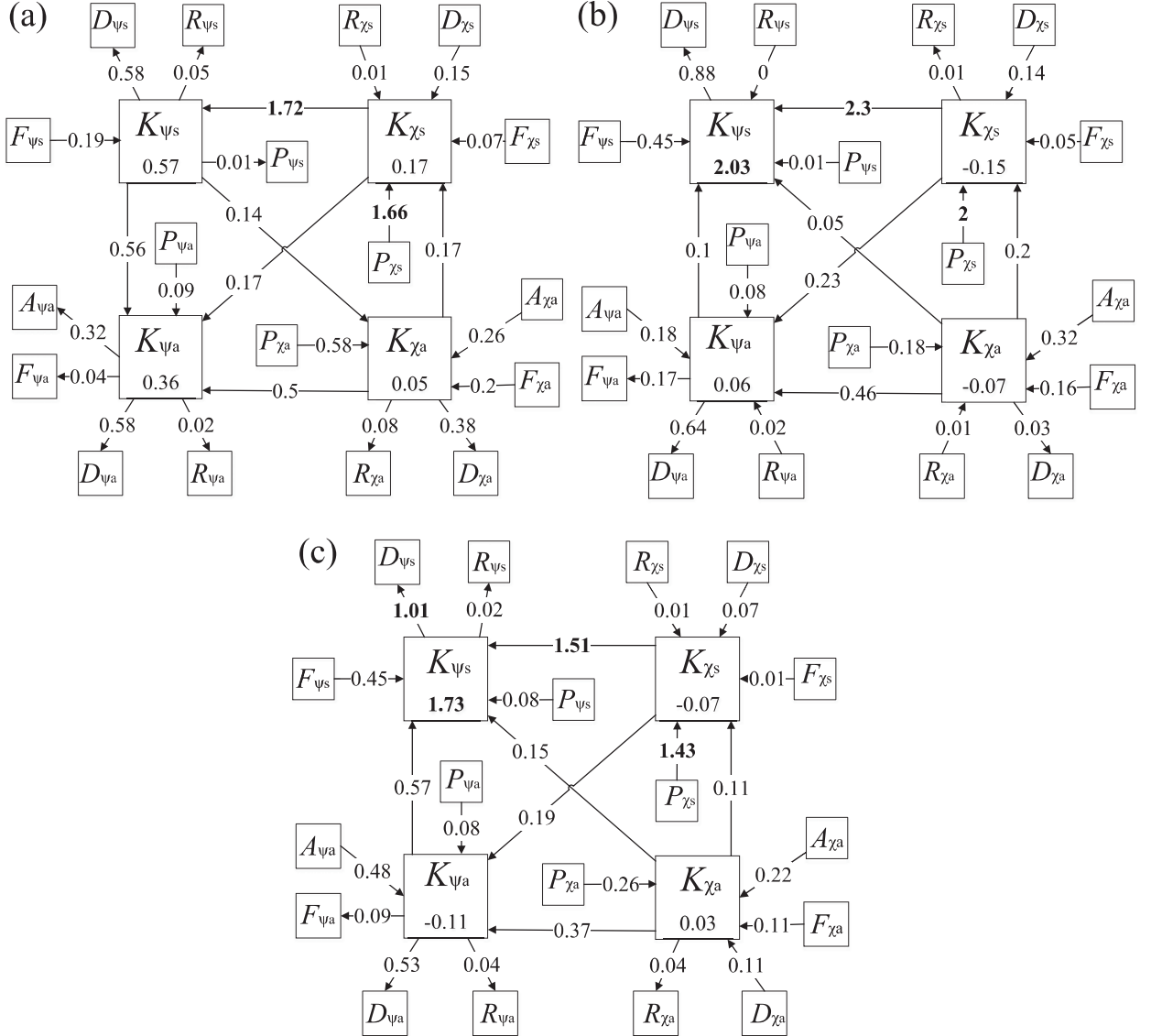


FIG. 17. As in Fig. 16, but for KE budgets vertically integrated through the midlevels ($\sigma = 0.785\text{--}0.44$, about 1900–6000 m AGL).

organized convection, instead of disorganized VHTs, and related latent heating may have contributed to the positive temperature anomalies (warm core).

5. Conclusions and discussion

Tropical cyclone genesis is a very important aspect of TC research and forecasting. The formation process of a TC is an evolution process from disorganized tropical disturbances (convection, including VHTs) to an approximately axisymmetric independent TC vortex with distinct energy transformations, which is still not well understood. In this study, a set of KE budget equations were derived to study the KE budget characteristics

during the genesis process of TC Durian from 1800 UTC 28 June to 1200 UTC 29 June 2001. High-resolution numerical simulation data by Zhang et al. (2008b) were used, which have been successfully applied to examining the features of multiple-scale systems in Durian's formation process (Zhang et al. 2008a, 2010). The genesis process was divided into three stages. Stage 1 was the monsoon trough stage, stage 2 was the MCV stage, and stage 3 was the establishment stage of the TC vortex. Horizontal wind fields were partitioned into four components, namely, the SRF, ARF, SDF, and ADF, to investigate the axisymmetrization process associated with TC genesis. The main results were as follows.

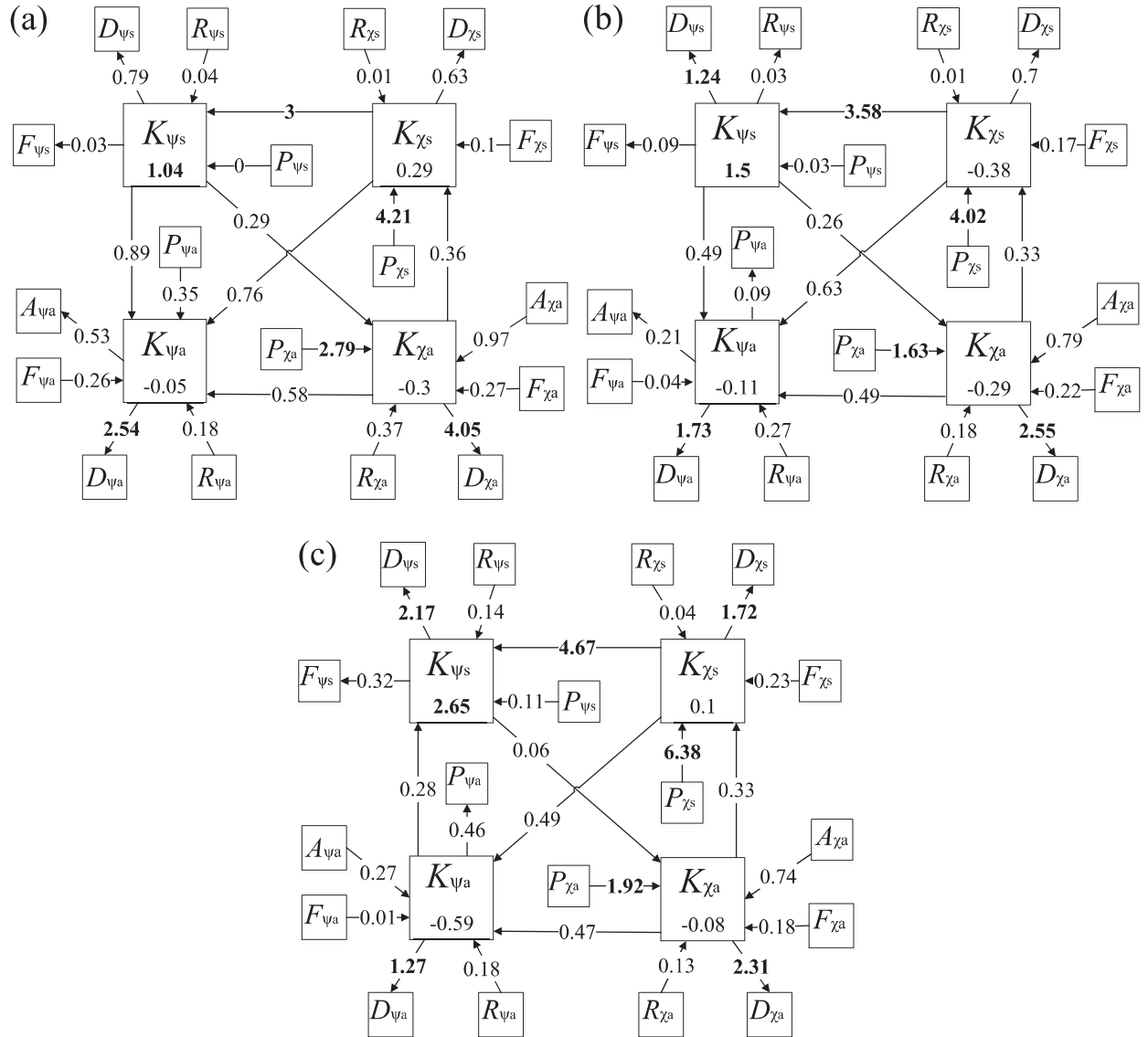


FIG. 18. As in Fig. 16, but for KE budgets vertically integrated through the lower levels ($\sigma = 0.995–0.855$, about 40–1240 m AGL).

- 1) The KE of the SRF was much larger than those of the other three flow components (ASF, SDF, and ADF), and kept on growing throughout the whole genesis period, and a larger growth rate was observed after 0000 UTC 29 June 2001 when the midlevel MCV developed rapidly and the surface TC vortex was about to establish. Most of the KE tendencies of the SRF were restricted to the mid- and lower levels, consistent with the fact that the midlevel MCV and the low-level TC vortex were the major systems during the three stages. The KE conversion from SDF, (K_{χ_s} , K_{ψ_s}), instead of the potential energy term (P_{ψ_s}), was always the main contributor to the KE tendencies of the SRF. Another conversion term

associated with K_{ψ_s} , (K_{ψ_a} , K_{ψ_s}), acted as a sink for the KE of the SRF in stage 1 before TC genesis and changed gradually to a weak source in stage 3 after the TC vortex developed. A significant increase in K_{ψ_s} in stage 2 was mainly related to the rapid development of the MCV at the midlevel and a slower development of low-level circulation, and the rapid increase in stage 3 was mainly associated with the establishment of the surface TC vortex and vertical coupling with the midlevel MCV.

- 2) A conceptual model of the KE budgets associated with the genesis process of TC Durian was proposed based on the analysis in this study. As the largest KE component, the KE of the SRF dominated the

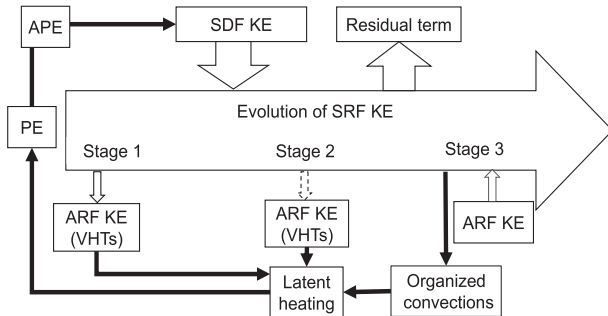


FIG. 19. A conceptual model of the KE budgets associated with the genesis process of TC Durian.

genesis (axisymmetrization) process of TC Durian. The KE of the SRF was always increasing in all three stages of the TC genesis, which was constantly and largely converted from the KE of the SDF. Furthermore, the KE of the SDF was largely converted from potential energy through baroclinic processes (P_{χ_s}). Based on the energy budget terms, it was found that during the genesis process of TC Durian, VHTs largely emerged in stages 1 and 2 in the favorable environment provided by the MCV. Massive latent heat was released to warm the atmosphere, which benefitted the accumulation of APE and the transformation from APE to KE. As a result of the growth of symmetric flow during stage 1 and energy conversion, symmetric rotational circulation strengthened at stage 2, especially at the midlevel. Impacted by the developing MCV, some VHTs started to aggregate and merge. In stage 3, the intensity of the VHTs and the diabatic heating rate decreased at the mid- to high level but not at the lower level. With increasing (decreasing) inward radial wind at the lower (mid-) level, the APE greatly converted to KE of the SDF, then to KE of the SRF at the lower level. Meanwhile, the TC vortex with a low central pressure and a warm core was set up, during which organized convection, instead of disorganized VHTs in the first two stages, and related latent heating may have contributed to the positive temperature anomalies (warm core) at the upper level.

Acknowledgments. Yaping Wang and Xiaopeng Cui are supported by the National Basic Research Program of China (973 Program) under Grant 2015CB452804, the National Natural Science Foundation of China under Grant 41175056, and the Shanghai Typhoon Research Foundation under Grant 2013ST01. Xiaofan Li is supported by the National Natural Science Foundation of China under Grant 41475039 and the National Key Basic Research Program of China under Grant

2015CB953601. Thanks also go to the anonymous reviewers who provided useful suggestions to thoroughly improve the manuscript.

REFERENCES

- Bister, M., and K. A. Emanuel, 1997: The genesis of Hurricane Guillermo: TEXMEX analyses and a modeling study. *Mon. Wea. Rev.*, **125**, 2662–2682, doi:[10.1175/1520-0493\(1997\)125<2662:TGOHGT>2.0.CO;2](https://doi.org/10.1175/1520-0493(1997)125<2662:TGOHGT>2.0.CO;2).
- Buechler, D. E., and H. E. Fuelberg, 1986: Budgets of divergent and rotational kinetic-energy during two periods of intense convection. *Mon. Wea. Rev.*, **114**, 95–114, doi:[10.1175/1520-0493\(1986\)114<0095:BODARK>2.0.CO;2](https://doi.org/10.1175/1520-0493(1986)114<0095:BODARK>2.0.CO;2).
- Carr, L. E., and R. T. Williams, 1989: Barotropic vortex stability to perturbations from axisymmetry. *J. Atmos. Sci.*, **46**, 3177–3191, doi:[10.1175/1520-0469\(1989\)046<3177:BVSTPF>2.0.CO;2](https://doi.org/10.1175/1520-0469(1989)046<3177:BVSTPF>2.0.CO;2).
- Chan, J. C. L., and K. K. W. Cheung, 1998: Characteristics of the asymmetric circulation associated with tropical cyclone motion. *Meteor. Atmos. Phys.*, **65**, 183–196, doi:[10.1007/BF01030787](https://doi.org/10.1007/BF01030787).
- Charney, J. G., and A. Eliassen, 1964: On the growth of the hurricane depression. *J. Atmos. Sci.*, **21**, 68–75, doi:[10.1175/1520-0469\(1964\)021<0068:OTGOTH>2.0.CO;2](https://doi.org/10.1175/1520-0469(1964)021<0068:OTGOTH>2.0.CO;2).
- Chen, T. C., and A. C. Wiin-Nielsen, 1976: On the kinetic energy of the divergent and nondivergent flow in the atmosphere. *Tellus*, **28**, 486–498, doi:[10.1111/j.2153-3490.1976.tb00697.x](https://doi.org/10.1111/j.2153-3490.1976.tb00697.x).
- Cheung, K. K. W., 2004: Large-scale environmental parameters associated with tropical cyclone formations in the western North Pacific. *J. Climate*, **17**, 466–484, doi:[10.1175/1520-0442\(2004\)017<0466:LEPAWT>2.0.CO;2](https://doi.org/10.1175/1520-0442(2004)017<0466:LEPAWT>2.0.CO;2).
- Ding, Y. H., and Y. Z. Liu, 1985a: On the analysis of typhoon kinetic energy, Part I Budget of total kinetic energy and eddy kinetic energy (in Chinese). *Sci. China B*, **10**, 956–966.
- , and —, 1985b: On the analysis of typhoon kinetic energy, Part II Conversion between divergent and nondivergent wind (in Chinese). *Sci. China B*, **11**, 1045–1054.
- Emanuel, K. A., 1986: An air-sea interaction theory for tropical cyclones. Part I: Steady-state maintenance. *J. Atmos. Sci.*, **43**, 585–605, doi:[10.1175/1520-0469\(1986\)043<0585:AASITF>2.0.CO;2](https://doi.org/10.1175/1520-0469(1986)043<0585:AASITF>2.0.CO;2).
- Feng, T., G. H. Chen, R. H. Huang, and X. Y. Shen, 2014: Large-scale circulation patterns favourable to tropical cyclogenesis over the western North Pacific and associated barotropic energy conversions. *Int. J. Climatol.*, **34**, 216–227, doi:[10.1002/joc.3680](https://doi.org/10.1002/joc.3680).
- Fu, S. M., J. H. Sun, S. X. Zhao, and W. L. Li, 2011: The energy budget of a southwest vortex with heavy rainfall over South China. *Adv. Atmos. Sci.*, **28**, 709–724, doi:[10.1007/s00376-010-0026-z](https://doi.org/10.1007/s00376-010-0026-z).
- Gray, W. M., 1968: Global view of the origin of tropical disturbances and storms. *Mon. Wea. Rev.*, **96**, 669–700, doi:[10.1175/1520-0493\(1968\)096<0669:GVOTOO>2.0.CO;2](https://doi.org/10.1175/1520-0493(1968)096<0669:GVOTOO>2.0.CO;2).
- , 1998: The formation of tropical cyclones. *Meteor. Atmos. Phys.*, **67**, 37–69, doi:[10.1007/BF01277501](https://doi.org/10.1007/BF01277501).
- Hendricks, E. A., M. T. Montgomery, and C. A. Davis, 2004: The role of “vortical” hot towers in the formation of Tropical Cyclone Diana (1984). *J. Atmos. Sci.*, **61**, 1209–1232, doi:[10.1175/1520-0469\(2004\)061<1209:TROVHT>2.0.CO;2](https://doi.org/10.1175/1520-0469(2004)061<1209:TROVHT>2.0.CO;2).
- Kornegay, F. C., and D. G. Vincent, 1976: Kinetic energy budget analysis during interaction of Tropical Storm

- Candy (1968) with an extratropical frontal system. *Mon. Wea. Rev.*, **104**, 849–859, doi:[10.1175/1520-0493\(1976\)104<0849:KEBADI>2.0.CO;2](https://doi.org/10.1175/1520-0493(1976)104<0849:KEBADI>2.0.CO;2).
- Lee, C. S., Y. L. Lin, and K. K. Cheung, 2006: Tropical cyclone formations in the South China Sea associated with the mei-yu front. *Mon. Wea. Rev.*, **134**, 2670–2687, doi:[10.1175/MWR3221.1](https://doi.org/10.1175/MWR3221.1).
- , K. K. Cheung, J. S. Hui, and R. L. Elsberry, 2008: Mesoscale features associated with tropical cyclone formations in the western North Pacific. *Mon. Wea. Rev.*, **136**, 2006–2022, doi:[10.1175/2007MWR2267.1](https://doi.org/10.1175/2007MWR2267.1).
- Li, A. B., L. F. Zhang, Z. L. Zang, and Y. Zhang, 2012: Computation of stream function and velocity potential in a limited area and its application to typhoon (in Chinese). *J. Meteor. Sci.*, **32**, 1–8.
- Li, X. F., and B. Wang, 1994: Barotropic dynamics of the beta-gyres and beta-drift. *J. Atmos. Sci.*, **51**, 746–756, doi:[10.1175/1520-0469\(1994\)051<0746:BDOTBG>2.0.CO;2](https://doi.org/10.1175/1520-0469(1994)051<0746:BDOTBG>2.0.CO;2).
- Li, Y., L. S. Chen, and J. Z. Wang, 2005: Diagnostic study of the sustaining and decaying of tropical cyclones after landfall (in Chinese). *Chin. J. Atmos. Sci.*, **29**, 482–490.
- Montgomery, M., M. Nicholls, T. Cram, and A. Saunders, 2006: A vortical hot tower route to tropical cyclogenesis. *J. Atmos. Sci.*, **63**, 355–386, doi:[10.1175/JAS3604.1](https://doi.org/10.1175/JAS3604.1).
- Palmen, E., 1948: On the formation and structure of tropical hurricanes. *Geophysica*, **3**, 26–38.
- Park, M.-S., H.-S. Kim, C.-H. Ho, R. L. Elsberry, and M.-I. Lee, 2015: Tropical Cyclone Mekkhala (2008) formation over the South China Sea: Mesoscale, synoptic-scale, and large-scale contributions. *Mon. Wea. Rev.*, **143**, 88–110, doi:[10.1175/MWR-D-14-00119.1](https://doi.org/10.1175/MWR-D-14-00119.1).
- Peng, J., M. S. Peng, T. Li, and E. Hendricks, 2014: Effect of baroclinicity on vortex axisymmetrization. Part II: Baroclinic basic vortex. *Adv. Atmos. Sci.*, **31**, 1267–1278, doi:[10.1007/s00376-014-3238-9](https://doi.org/10.1007/s00376-014-3238-9).
- Peng, M. S., J. Y. Peng, T. Li, and E. Hendricks, 2014: Effect of baroclinicity on vortex axisymmetrization. Part I: Barotropic basic vortex. *Adv. Atmos. Sci.*, **31**, 1256–1266, doi:[10.1007/s00376-014-3237-x](https://doi.org/10.1007/s00376-014-3237-x).
- Riehl, H., 1948: On the formation of typhoons. *J. Meteor.*, **5**, 247–265, doi:[10.1175/1520-0469\(1948\)005<0247:OTFOT>2.0.CO;2](https://doi.org/10.1175/1520-0469(1948)005<0247:OTFOT>2.0.CO;2).
- Ritchie, E. A., and G. J. Holland, 1997: Scale interactions during the formation of Typhoon Irving. *Mon. Wea. Rev.*, **125**, 1377–1396, doi:[10.1175/1520-0493\(1997\)125<1377:SIDTFO>2.0.CO;2](https://doi.org/10.1175/1520-0493(1997)125<1377:SIDTFO>2.0.CO;2).
- , and —, 1999: Large-scale patterns associated with tropical cyclogenesis in the western Pacific. *Mon. Wea. Rev.*, **127**, 2027–2043, doi:[10.1175/1520-0493\(1999\)127<2027:LSPAWT>2.0.CO;2](https://doi.org/10.1175/1520-0493(1999)127<2027:LSPAWT>2.0.CO;2).
- Rotunno, R., and K. A. Emanuel, 1987: An air-sea interaction theory for tropical cyclones. Part II: Evolutionary study using a nonhydrostatic axisymmetric numerical model. *J. Atmos. Sci.*, **44**, 542–561, doi:[10.1175/1520-0469\(1987\)044<0542:AAITFT>2.0.CO;2](https://doi.org/10.1175/1520-0469(1987)044<0542:AAITFT>2.0.CO;2).
- Sun, Y., Z. Zhong, and Y. Wang, 2012: Kinetic energy budget of Typhoon Yagi (2006) during its extratropical transition. *Meteor. Atmos. Phys.*, **118**, 65–78, doi:[10.1007/s00703-012-0200-1](https://doi.org/10.1007/s00703-012-0200-1).
- Wang, L., and K. H. Lau, 2011: Statistical analysis of tropical disturbances over the South China Sea during 1997–2006. *J. Ocean Univ. China*, **10**, 99–105, doi:[10.1007/s11802-011-1733-5](https://doi.org/10.1007/s11802-011-1733-5).
- , R. H. Huang, and R. G. Wu, 2013: Interdecadal variability in tropical cyclone frequency over the South China Sea and its association with the Indian Ocean sea surface temperature. *Geophys. Res. Lett.*, **40**, 768–771, doi:[10.1002/grl.50171](https://doi.org/10.1002/grl.50171).
- Wang, L. J., S. Lu, Z. Y. Guan, and J. L. He, 2010: Large scale circulation features of the maintenance and increase in torrential rains from the landing typhoon Durian (in Chinese). *Climatic Environ. Res.*, **15**, 511–521.
- Yao, C., 2003: Variations of typhoon Durian (0103) intensity and analysis of the heavy rain causes (in Chinese). *J. Trop. Meteor.*, **19**, 180–188.
- Yi, B. Q., A. K. H. Lau, A. M. Liang, and Q. H. Zhang, 2008: Numerical study of the genesis and development of typhoon Wukong (2000) over South China Sea (in Chinese). *Acta Sci. Natural. Univ. Pekinensis*, **44**, 773–780.
- Zehr, R., 1992: Tropical cyclogenesis in the western North Pacific. NOAA Tech Rep. NESDIS 61, 181 pp.
- Zhang, D. L., and N. Bao, 1996: Oceanic cyclogenesis as induced by a mesoscale convective system moving offshore. Part II: Genesis and thermodynamic transformation. *Mon. Wea. Rev.*, **124**, 2206–2226, doi:[10.1175/1520-0493\(1996\)124<2206:OCAIBA>2.0.CO;2](https://doi.org/10.1175/1520-0493(1996)124<2206:OCAIBA>2.0.CO;2).
- Zhang, Q. H., and C. R. Guo, 2008: Overview of the studies on tropical cyclone genesis (in Chinese). *Acta Ocean. Sin.*, **30**, 1–11.
- Zhang, W. L., and X. P. Cui, 2013: Review of the studies on tropical cyclone genesis (in Chinese). *J. Trop. Meteor.*, **29**, 337–346.
- , —, A. S. Wang, and Z. P. Zong, 2008a: Numerical simulation of hot towers during pre-genesis stage of Typhoon Durian (2001) (in Chinese). *J. Trop. Meteor.*, **24**, 619–628.
- , A. S. Wang, and X. P. Cui, 2008b: The role of the middle tropospheric mesoscale vortex in the genesis of Typhoon Durian (2001)—Simulation and verification (in Chinese). *Chin. J. Atmos. Sci.*, **32**, 1197–1209.
- , X. P. Cui, and J. X. Dong, 2010: The role of the middle tropospheric mesoscale vortex in the genesis of Typhoon Durian (2001)—Diagnostic analysis of simulated data (in Chinese). *Chin. J. Atmos. Sci.*, **34**, 45–57.